Journal of Radiation Research and Applied Sciences 18 (2025) 102007

Contents lists available at ScienceDirect

Journal of Radiation Research and Applied Sciences

journal homepage: www.journals.elsevier.com/journal-of-radiation-research-and-applied-sciences

Multispectral remote sensing and radiometric data for delineating radioelement-enriched zones and their health hazards in Um Domi area, South Eastern Desert, Egypt

El Saeed R. Lasheen [a,*], Basma A. El-Badry [b], Samir Z. Kamh [c], Mabrouk Sami [d], Naglaa AbdelAll [b], Ioan V. Sanislav [e], Samia S. Hasan [f], Gehad M. Saleh [g]

[a] Geology Department, Faculty of Science, Al-Azhar University, Cairo, 11884, Egypt
[b] Physics Department, Faculty of Science, Imam Mohammad Ibn Saud Islamic University (IMSIU), Riyadh, Saudi Arabia
[c] Geology Department, Faculty of Science, Tanta University, Tanta, 31527, Egypt
[d] Geosciences Department College of Science, United Arab Emirates University, 15551, Al Ain, United Arab Emirates
[e] Economic Geology Research Centre (EGRU), College of Science and Engineering, James Cook University, Townsville, QLD, 4811, Australia
[f] Desert Research Center, El Matareya, Cairo Governorate, 11753, Egypt
[g] Nuclear Materials Authority. P. O. Box 530, El-Maadi, Cairo, Egypt

ARTICLE INFO

Keywords:
Radioactivity
Health assessment
Trachytic rocks
Remote sensing
Lineament density
Major faults

ABSTRACT

This study combines fieldwork, remote sensing methods, petrographic, and detection radioactive prospective of the Um Domi rocks to enhance the lithological characterization and deduce the possible harmful effects of radiation exposure on human health. In addition to determine the amounts of ^{40}K, ^{238}U, and ^{232}Th radiation present in these rocks, a number of radiological risk factors are assessed in order to determine the possible negative health effects of radiation exposure. Um Domi trachyte possesses an elevated concentrations of ^{40}K (1142.45 ± 181.46 Bqkg^{-1}), ^{238}U (1196.60 ± 323.52 Bqkg^{-1}), and ^{232}Th (755.08–444.32 Bqkg^{-1}) together with the overall amount (avg. 1897.53 ± 577.03 Bqkg^{-1}) employing the NaI (Tl) spectrometer. These outcomes surpass the accepted international norms. A number of radiological components have been used to evaluate the hazard associated with these rocks, and they showed high values relative to the international norms, suggesting substantial impact on the spontaneous gamma radiation released. Utilizing multispectral remote sensing data, it's observed that the clay and OH-bearing minerals are concentrated over granitic rocks, trachyte, and around Um Domi, whereas the altered products of Fe minerals are distributed around the ring of Um Domi. Importantly, it is noticed that the radioactive rich samples are located in the zone of moderate to high concentration of clay and Fe minerals. Additionally, by integrating the potential source rock, high alteration zones, lineament density, major faults, and rock samples containing radioactive mineralization, we can deduced that the radiation potential are structurally controlled.

1. Introduction

Exposure to radiation is inevitable for humans, and naturally generated radioactive elements play a major role. Human health is at risk due to this generated radiation, which also pollutes the environment. Rock, soil, water, and air can all contain this type of radiation (Akkurt & Günoğlu, 2014). The main radioactive fallout sources in soil/rocks include U, Th, K, and related decay derivatives. Accumulation and weathering are common activities that gradually increase radionuclides, particularly in the later magmatic phases. Compared to igneous rock, sedimentary rocks have lowered radiation emissions. In addition to natural radioactivity, humanity also contributes to earth's radioactivity, mostly via the widespread use of fertilizers made of phosphates and waste from factories. Due to the regional variation in external gamma dose rates, radionuclide spectra are essential for monitoring natural radioactivity. The amount of radionuclides that naturally exist in rocks determines these dosages (Abdul Sani et al., 2022; Al-Hamarneh & Awadallah, 2009; Al-Trabulsy et al., 2011; Krebs et al., 2019; Yıldırım & Gülmez, 2025). Soil-emitted radiation adds to the overall dose absorbed by food, inhalation, and others. Long-term

* Corresponding author.
E-mail address: elsaeedlasheen@azhar.edu.eg (E.S.R. Lasheen).

https://doi.org/10.1016/j.jrras.2025.102007
Received 26 July 2025; Received in revised form 2 September 2025; Accepted 6 October 2025
Available online 15 October 2025

ingestion of U and Th, as well as through inhalation, may trigger a variety of health issues, such as acute leukopenia, anemia, and chronic lung diseases; and Th exposure can trigger leukemia, liver, and lung cancers (Abdel-Aal et al., 2024; Kanmi et al., 2025; Qureshi et al., 2014; Raghavendra et al., 2019; Saleh, Lasheen, et al., 2025; Özden et al., 2023). Numerous studies have been conducted all around the world to ascertain the rocks' total radiation quantity (Abdul Sani et al., 2022; Al-Hamarneh & Awadallah, 2009; Al-Mur et al., 2025; Khaleal et al., 2023; Lasheen et al., 2025; Li et al., 2024; Saleh, Lasheen, et al., 2025; Shahrokhi et al., 2020; Shehzad et al., 2019; Özden & Aközcan, 2021).

From the other hand, the Egyptian crystalline rocks cover the northern sector of the ANS (Arabian Nubian Shield) (Saleh, Kamar, et al., 2025). These rocks include ophiolites, arc-related, granitic suites, and volcanic rocks. Furthermore, the bulk of these rocks survived the ore mining; they can be utilized for building parts in cement as well as stones for ornamentation due to their attractive forms and remarkable strength (Lasheen et al., 2024; Rashwan et al., 2023). Volcanic activity in Egypt spanned a long period and marked a change in tectonic setting from ocean floor and subduction-related volcanics in the Precambrian to intraplate volcanicity in the Phanerozoic. The influence of these complex tectonic regimes is reflected in time-related changes in the composition of the evolved rocks. During the Phanerozoic, continental intraplate volcanic activity in Egypt was intermittent and resulted in the extrusion of volcanic rocks of wide compositional variation, size, and mode of eruption (M. M. A. Adam et al., 2022; Lasheen et al., 2024). Geochronological studies on these Phanerozoic volcanics (Satir et al., 1991; Ressetar et al., 1981) revealed three phases of activity in Egypt. These are, Paleozoic (233–395 Ma), Mesozoic (74–191 Ma) and Tertiary (15–48 Ma). The plugs are part of the tectono-magmatic events that had affected the Eastern Desert of Egypt during the Mesozoic. Generally, the origin of continental intraplate alkaline rock series ranging from mildly alkaline or transitional basalts to peralkaline trachyte or rhyolites is a complex process and has been a matter of considerable investigation during the last two decades. Several evolutionary and petrogenetic models have been considered, a) crystal fractionation of Mantle-derived magma, b) interaction of mantle-derived magmas with crustal materials to produce trachyte melts (Davidson & Wilson, 1989), c) a magma mixing process (Gourgaud & Maury, 1984), and d) partial melting of the lower crust induced by the injection of volatile-rich basic magma of mantle origin. The alkaline volcanic rocks seem to host uranium are more than sub-alkaline and calc-alkaline varieties (Maithani & Srinivasan, 2011).

Remote sensing technologies provide powerful tools for geological mapping, offering rapid and cost-effective data acquisition and analysis across extensive and often inaccessible terrains. Multispectral and hyperspectral satellite data, particularly from platforms such as ASTER, Landsat-8, and Sentinel-2 have been widely utilized for lithological, structural, and mineralogical mapping in diverse geological settings (Acker et al., 2008; Gupta, 2003; Khaleal et al., 2024; A. Pour et al., 2019; A. B. Pour et al., 2018). These techniques are especially valuable in overcoming the limitations of conventional field-based methods, which can be logistically challenging and financially demanding over large areas (Masoumi et al., 2017). Among the most impactful remote sensing applications in mineral exploration are the detection of hydrothermal alteration minerals, lithological unit discrimination, and the extraction of structural lineaments (A. B. Pour et al., 2018). Numerous studies have demonstrated the effectiveness of Landsat-8 and ASTER imagery in identifying lithological variations and hydrothermal alteration zones that are indicative of potential mineralization sites (Hamdani & Baali, 2019; Khaleal et al., 2024; A. Pour et al., 2019; Sadek et al., 2020).

This study focuses on identify rock units through fieldwork and petrography, and to analyze the radioactive potential of the Um Domi rocks. Additionally, remote sensing datasets were used to enhance the lithological characterization of the study area. This has been achieved through the application of advanced Python-based remote sensing techniques in combination with petrographic analyses, providing a comprehensive and modern approach to lithological mapping and mineral exploration. Besides, measuring the concentrations of ^{232}Th, ^{238}U, and ^{40}K radiation in these rocks, the possible harmful effects of radiation exposure on human health are assessed using a variety of radiological risk indicators.

2. Field geology

The Phanerozoic Um Domi trachyte exposure is situated in the extreme southern part of Egypt's South Eastern Desert (Fig. 1). This trachyte plug, is semi-rounded in shape and covering approximately 0.8 km^2, rises to an elevation of 780 m above sea level. It is positioned between two conjugate wrench fault systems trending N–S and NW–SE. The region is extensively dissected by strike-slip faults oriented NE–SW, NW–SE, and N–S, with prominent displacements observed along the principal Wadis. The trachyte plug is fine-grained, fractured, intensely sheared, particularly along its contact with the surrounding granitic, metavolcanics, and gabbro that are intruded by quartz veins (Fig. 2a). Visible sulfide mineralization is common. The dominant alteration processes include hematitization, kaolinitization, and albitization. Joints are the most prevalent secondary structures, notably within the trachyte plug, with some joint sets (NW-SW, N–S and E–W) infilled by secondary minerals such as limonite and hematite, especially in the central portion of the plug. Small and unmapped volcanogenic sediments and mudstone can be recorded in the study area.

3. Methodology

3.1. Field and petrography

Over twenty-five samples were collected during a single field trip from Um Domi outcrops. Fourteen thin slices were made in order to identify the key minerals and their textures. (Fig. 3).

3.2. Mineralogy

The isolated minerals were examined by the environmental scanning electron microscope (ESEM) supported by energy dispersive spectrometer (EDS) unit.

3.3. Radioactive detection

To create radioactive equilibrium, ten rock samples (about 350 g each) from the Um Domi outcrops were air-dried, sieved to less than 200 mesh, put in 200 mL containers made of plastic, and packed for a period of at least 20 days (Fig. 3). Gamma-ray measurements were conducted using a Bicron NaI(Tl) spectrometer equipped with a 76 × 76 mm scintillation crystal and a photomultiplier tube housed in an aluminum casing. Radioactivity was assessed across three energy windows: 1460.8 keV for ^{40}K, 238.6 keV corresponding to ^{212}Pb for estimating ^{232}Th, and 92.6 keV corresponding to ^{234}Th for estimating ^{238}U. With counting errors of 1–5 %, the minimum measurable concentrations are around 0.4 ppm U, 0.6 ppm Th, and 0.1 % K. Strict energy-calibration processes that account for potential peak interferences preserve precision.

Apply the following formulas to assess the radiological effects of samples: H_{ex} & H_{in} exterior & internal indicators; H_γ, gamma index; R_{aeq}, radium equivalent; ELCR, excess life-time cancer; D, rate of absorbed dose; $AED_{out\ \&}$ in, outdoor and indoor annual dosage. The designations for ^{232}Th, ^{40}K, ^{238}U, and activity are R_{Th}, R_K, and R_U, in that order.

$$D\ (nGy\ h^{-1}) = 0.430\ R_U + 0.666\ R_{Th} + 0.042 R_K \text{ (European Commission, 1999)} \quad (1)$$

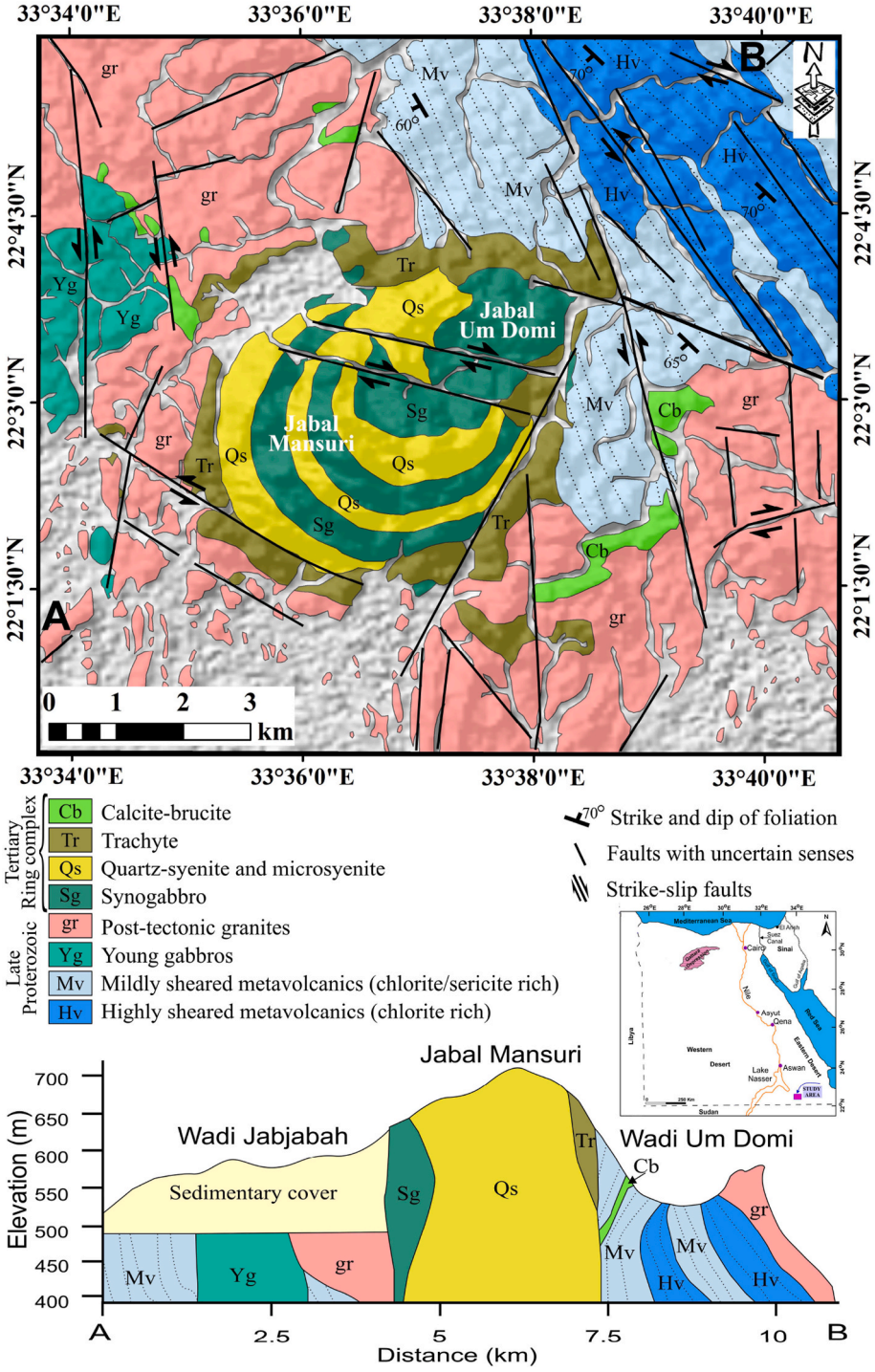

Fig. 1. Um Domi area geologic map, south Eastern Desert, Egypt (EGSMA, 1996; Saleh et al., 2023). Inset location map and geologic cross section.

$$AED\left(\frac{mSv}{y}\right)=\sum\left(D\left(\frac{nGy}{h}\right)\times 0.7\left(\frac{Sv}{Gy}\right)\times occupancy\,factor\right)\times 8760h\times 10^{-6}\,(\text{UNSCEAR, 2010})$$ in which the occupancy index is 0.2 for outside and 0.8 for inside occupancy period (2)

$$H_{in}\ \&\ H_{ex=}R_U/185\ (370\ \text{for outdoor})+R_{Th}/259+R_K/4810\ (\text{UNSCEAR, 2010})$$ (3)

$$I\gamma = R_{Ra}/300+R_{Th}/200+R_K/3000\ (\text{European Commission, 1999})$$ (4)

$$Ra_{eq}\ (Bq.kg^{-1}) = R_U + 1.43\ R_{Th} + 0.077\ R_K\ (\text{UNSCEAR, 2010; Yu et al., 1992})$$ (5)

$$ELCR(mSv/y) = AED\ x\ DL\ (70\ years) x\ RF\ \left(0.05\ Sv^{-1}\right)\ (\text{Taskin et al., 2009; UNSCEAR, 2010})$$ (6)

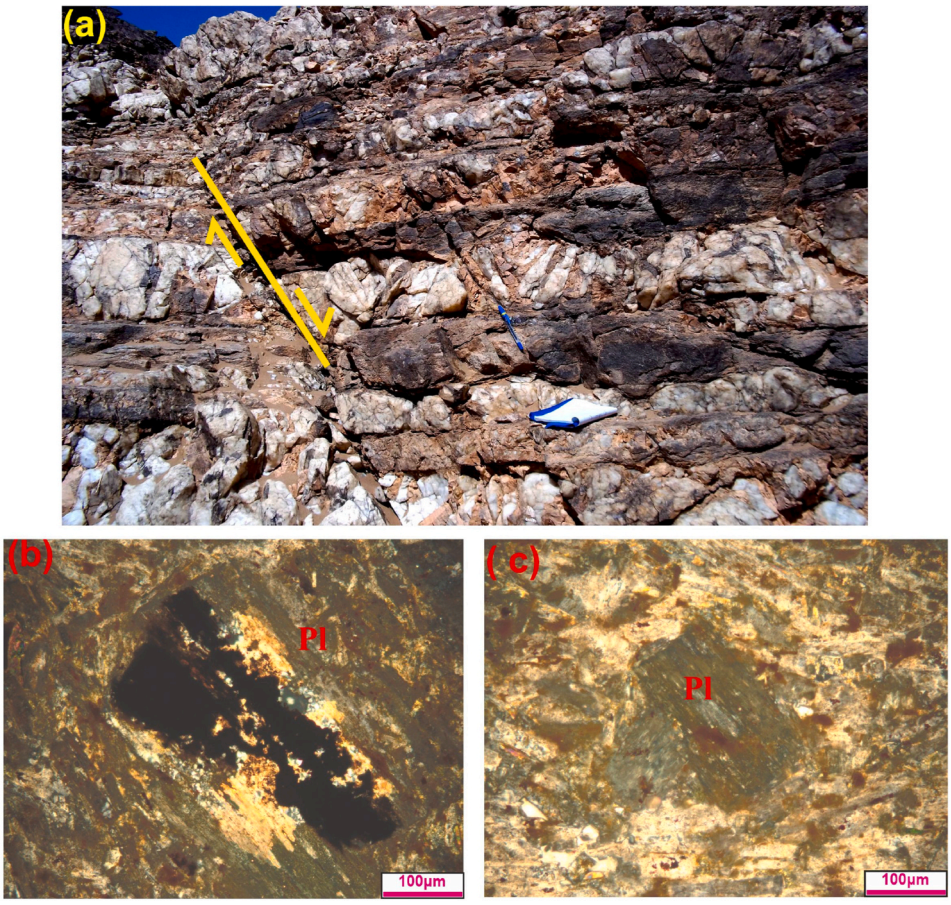

Fig. 2. Field photo shows: **a)** Net of faulted quartz veins intruding trachyte plug; and microscopic micrographs reveal: **b-c**) Phenocrystal and laths of oligoclase forming trachytic texture.

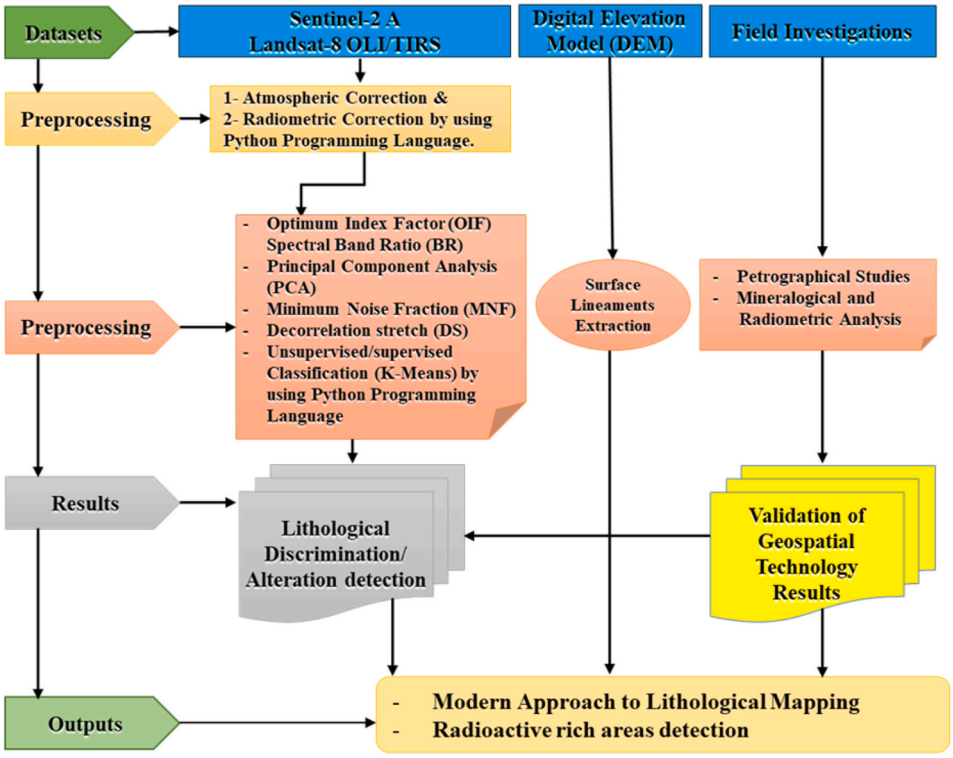

Fig. 3. Flowchart of the adopted methodology in the present study.

3.4. Remote sensing data

A structured image processing workflow was adopted to enhance lithological discrimination in the study area using the Digital Elevation Model (DEM) and multi-spectral Sentinel-2 imagery from Sentinel hub site (https://dataspace.copernicus.eu/analyse/apis/sentinel-hub) (Fig. 3). The remotely sensed data analysis included many techniques: Digital Elevation Model (DEM), Optimum Index Factor (OIF) computation, spectral band ratio generation, Principal Component Analysis (PCA), Minimum Noise Fraction (MNF) Decorrelation Strech (DS), supervised and unsupervised classification. All processing steps were performed using the Python programming language, which provides a flexible, reproducible, and open-source environment for advanced geospatial analysis (Gorelick et al., 2017). A DEM with a spatial resolution of 30 m was downloaded from the open topography platform (https://opentopography.org/) to support the geomorphological and structural analysis of the Gebel Um Domi area, South Eastern Desert of Egypt. OIF was computed to identify the most suitable RGB band combinations that maximize spectral variability and minimize redundancy. The OIF was calculated for all possible three-band combinations using the following formula (Jensen, 2005):

$$OIF = (\sigma_i + \sigma_j + \sigma_k) / (|\rho_{ij}| + |\rho_{ik}| + |\rho_{jk}|)$$

Where: σ_i, σ_j, σ_k: Standard deviation of bands B_i, B_j, and B_k respectively. ρ_{ij}, ρ_{ik}, ρ_{jk}: Pearson correlation coefficients between bands B_i & B_j, B_i & B_k, and B_j & B_k. $|\rho|$: Absolute value of the correlation coefficient, indicating the degree of redundancy. Python's numpy and itertools libraries were used to implement the automated analysis. The B5–B6–B7 combination exhibited the highest OIF value, suggesting superior suitability for lithological interpretation in RGB display, which agrees with findings by Nafigin et al. (2022) and Pour and Hashim (2012).

Several spectral band ratios were calculated to enhance lithological contrasts based on known reflectance characteristics: B7/B5 of Sentinel-2 highlights felsic intrusive rocks (trachyte plugs); B6/B7 of Landsat-8 which sensitive to clay-altered volcanic rocks and B4/B2 of Landsat-8 enhances ferruginous materials. These ratios were implemented using rasterio and numpy, and then saved as Geo TIFFs. Similar band ratio approaches have been validated in geological remote sensing studies (Pour & Hashim, 2012; Sabins, 1999).

To reduce data dimensionality and emphasize major spectral variance, PCA was applied to bands B2, B4, B5, B6, and B7 of Sentinal-2 and bands B1 to B7 of Landsat-8. The analysis was conducted using the PCA module from Python's scikit-learn package. The first three components were retained, capturing most of the spectral variability. These components proved useful for enhancing structural and lithological boundaries (Kasperek & Podpora, 2024). An unsupervised K-Means clustering algorithm was applied directly to six Sentinel-2 bands (B2, B3, B4, B8, B11, and B12), after resampling the 20-m resolution bands (B11 and B12) to 10-m resolution to ensure spatial consistency. The classification was executed using the K-Means implementation from scikit-learn, resulting in four spectral clusters that capture lithological variability across the scene. This direct use of multi-band reflectance values as input to clustering follows methodologies established in Pour et al. (2018) and Pour and Hashim (2012). In addition to refining the lithological discrimination two supervised classification techniques, the maximum likelihood classification (MLC) and the support vector machine (SVM) were performed to the Landsat-8 data. The alteration zone and altered minerals were paid attention due to their high potential of radioactive contents.

The entire processing chain was executed using Python, offering key benefits: Open-source: Free and community-supported tools (rasterio, numpy, scikit-learn); Automation: Scripting allows repeatability and customization; Integration: Seamless combination of analysis, visualization, and machine learning; Cloud-ready: Executed via Google Colab for accessibility and performance (Gorelick et al., 2017). Python is increasingly adopted in remote sensing research due to its scalability and scientific robustness (Chen et al., 2022; Farahbakhsh et al., 2025).

4. Results

4.1. Petrography

Mineralogical and textural investigations of the Gabal Um Domi trachyte plug reveal that it is fine-grained and exhibits pinkish-grey to brown coloration. The rock is primarily composed of quartz, plagioclase, alkali amphiboles, alkali feldspars, and alkali pyroxene, set within a fine-grained groundmass characterized by a distinct trachytic texture (Fig. 2b–c). Accessory minerals include kasolite, uranothorite, zircon, apatite, and opaque phases. Quartz appears as small subhedral to anhedral grains within the groundmass and frequently hosts inclusions of zircon and apatite. Feldspars are mainly represented by subhedral sanidine and orthoclase perthite. Oligoclase occurs as euhedral to subhedral phenocrysts and laths, displaying lamellar twinning and zoning. Alteration features include sericitization and kaolinitization, often along the core or crystal margins. Alkali amphiboles are dominated by riebeckite, with minor arfvedsonite crystals. Aegirine commonly rims arfvedsonite, forming characteristic snowball textures. Apatite is observed as fine prismatic or acicular crystals, while zircon appears as slender prisms in the groundmass and as inclusions in quartz. Opaque minerals form anhedral grains, occasionally clustering around feldspar crystals or forming aggregates.

4.2. Mineralogy

The isolated and detected minerals using ESEM and EDS are kasolite, uranothorite, zircon, and galena minerals.

Kasolite [$Pb(UO_2)(SiO_4)*H_2O$] is a secondary mineral that results from uranite oxidation. Kasolite is characterized by its stout prismatic, greasy luster, and color variation from yellow to brownish yellow, amber brown, lemon yellow, green, or reddish orange. The ESEM techniques certified that kasolites consist essentially of U and Pb (Fig. 4a).

Uranothorite [(Th, U, Ce) SiO_4] exhibits dark brown and brownish to pale-brownish color. The SEM data of examined uranothorite shows that the presence of Th, U, and Si as the main constituents (Fig. 4b).

Zircon [$Zr(SiO_4)$] varies from short prismatic crystals to euhedral dull edges. Deer et al., 1992) concluded that zircon sometimes gives rise to pleochroic haloes due to its content of radioactive elements. The SEM data (Fig. 4c) shows that it consists essentially of Zr and Si.

Galena (PbS) shows a dark grey color and has a metallic luster and dark grey streak and is sometimes altered to hematite and goethite. The SEM data of galena shows that the Pb and S are the main components (Fig. 4d).

4.3. Radionuclides abundance

For ten samples obtained from the Um Domi region, the amounts and concentrations of the radioactive elements ^{40}K, ^{238}U, and ^{232}Th have been established (Table 1). These samples' average ± SD findings are higher above the nationwide record level. As shown above (Table 1), the samples taken from the Um Domi region actually show a development of their level of activity: The minerals that contain potash and are associated with greater K activity are $^{40}K > {}^{238}U > {}^{232}Th$ (Abdel-Aal et al., 2024; Li et al., 2024; Ramola et al., 2011; Shahrokhi et al., 2020; Zakaly et al., 2024). The rocks under examination have ^{238}U (1196.60 ± 323.52 $Bqkg^{-1}$), ^{232}Th (755.08 ± 444.32 $Bqkg^{-1}$), and ^{40}K (1142.45 ± 181.46 $Bqkg^{-1}$) that are above the worldwide monitoring limit, according to the NaI (Tl) analyzer. The presence of radioactive minerals including zircon, uranothorite, kasolite, and titanite, which contain radionuclides in their framework, may be the cause of these elevated amounts (European Commission, 1999; Kanmi et al., 2025; Li et al., 2024; Pavlidou et al.,

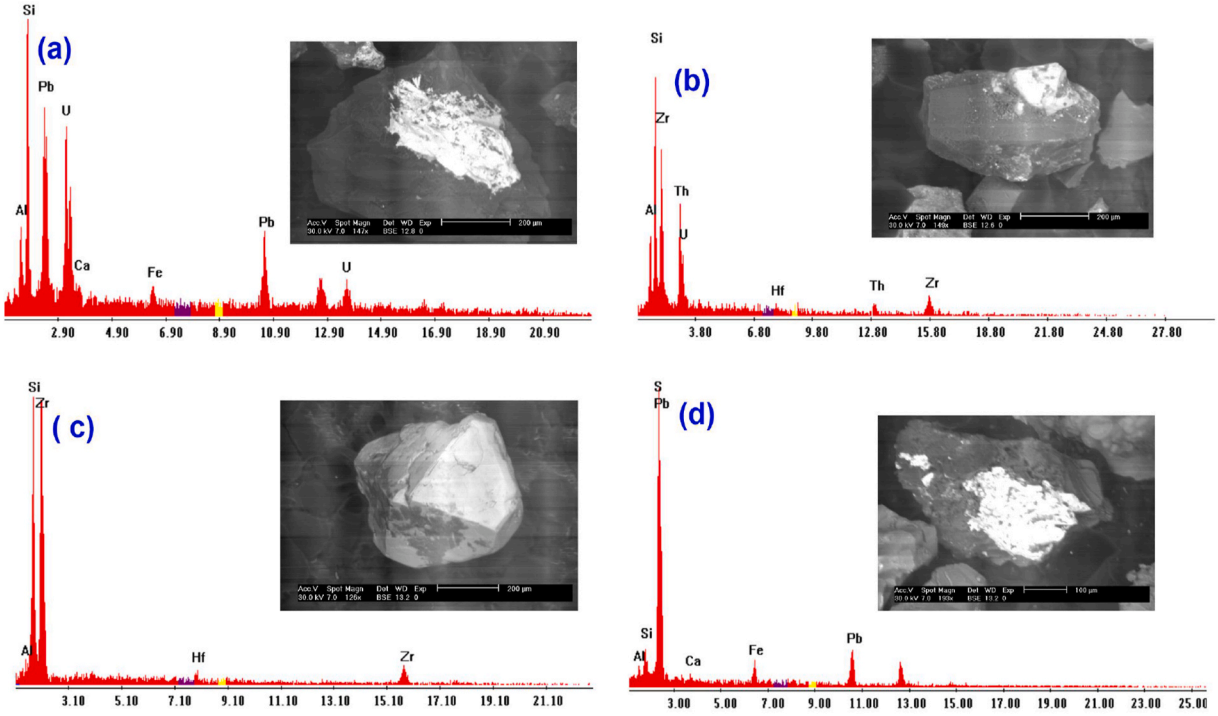

Fig. 4. The patterns of EDX and BSE images of: **a**) Kasolite, **b**) Uranothorite, **c**) Zircon, and d) Galena minerals.

2006; Sahoo et al., 2011; Sivakumar et al., 2018; Yu et al., 1992). Table 1 shows that the greatest Th/K (average 0.64), over the global limit of 0.07, is found in the Um Domi trachyte rocks. This might be explained by the high potassium content caused by K-metasomatism in these rocks. While the global average is 3.94, their Th/U ratio is low (avg. 0.63). The smallest results show U migration in proportion to Th in these rocks, as they are associated with a high U quantity relative to Th in the analyzed samples. This results from the deposition of secondary U during hydrothermal process (Kanmi et al., 2025; Khandaker et al., 2025; Qureshi et al., 2014; UNSCEAR, 2000).

The distribution histogram of ^{238}U, ^{232}Th, and ^{40}K activity concentrations is revealed in Fig. 5. The distribution frequency is seen as normal for ^{238}U, while ^{232}Th, and ^{40}K described the multi-modality degree. This multi-modality property is due to different minerals; zircon, kasolite, and uranothorite. However, the higher concentrations of uranium are attributed to the presence of radioactive minerals that deposited as a result of hydrothermal processes causing remobilizing of uranium minerals. Box plots of concentrations and radiological norms were created for the assessed rocks as given in Fig. 6, where the data group's lowest and highest values are indicated by the two ends of the boxes. The median, which separates the data so that 50 % of the values are below and 50 % are above it, is indicated by the line inside box. ^{238}U reveals a wide variation relative to ^{40}K and ^{232}Th. Although ^{232}Th has the lowest variation, there is one sample (no UD9) plot outliers due to high content of ^{232}Th ~2000 Bqkg^{-1}, due to enrichment of uranothorite minerals.

A popular statistical technique for figuring out whether a dataset has a normal distribution is the Shapiro-Wilk test (Kanmi et al., 2025). The results of the Shapiro-Wilk test are corroborated by the normal probability map in Fig. 7. The ^{238}U data points resemble a straight line, indicating that these characteristics have a normal distribution. On the other hand, the ^{40}K and ^{232}Th points show a non-normal distribution, as they diverge from a straight line.

The results of this investigation (^{40}K, ^{232}Th, and ^{238}U) are compared to global standards in Table 2. The concentrations that have been assessed are higher than UNSCEAR (2010) legal limit, as well as those of Sapin granites (Guillén et al., 2014), Rize Province (Yuan et al., 1995), Yelagiri Hills (Wais et al., 2023), Jeddah coastline (Al-Mur et al., 2025), Oyun of Nigeria (Kanmi et al., 2025), Sharm El Luli coastline (Saleh, Lasheen, et al., 2025), granitic rocks (Sharaf & Hamideen, 2013), Irepodun rocks (Kanmi et al., 2025), Wadi El- Gemal sediments (Khaleal et al., 2023), West coast sediment (Malain et al., 2010), and rock materials (Senthilkumar et al., 2014). In contrast, these concentrations are close to those of Kuzmanović et al. (2024), and Tuo et al. (2020), which are higher than the legal limit of UNSCEAR (2010).

4.4. Remotely sensed data analysis

4.4.1. Lineaments and structural features extraction

This dataset provided high-quality elevation information that enabled detailed surface analysis. Using the DEM, surface lineaments and structural features were extracted through a combination of visual interpretation and GIS-based techniques. The orientation of these features was further analyzed using rose diagrams, which indicated three predominant structural trends: NE-SW, NW-SE, N-S, and E-W. These trends reflect the tectonic framework influencing the region and align with previously reported structural patterns in the ANS (Fig. 8a and b). The concentration and the intersection of these linear fractures help greatly in the formation of the alteration zone in turn in the concentration of the radioactive materials.

4.4.2. Band combination and Optimum Index Factor (OIF)

The OIF was computed for all possible 3-band combinations among bands B2 to B7 of Sentinal-2. The combination B5–B6–B7 achieved the highest OIF value (5061.44) (Table 3, Fig. 9a), indicating the greatest spectral variability and the lowest correlation among its bands. This suggests that it is the most informative combination for RGB display and initial lithological interpretation. Other high-performing combinations included B4-B5-B6 (Fig. 9b), supporting the significance of shortwave infrared bands in geological mapping. These results were used to construct an RGB composite image using bands B5 (Red), B6 (Green), and B7 (Blue) to enhance lithological contrast in further interpretation and classification stages (Fig. 9a). High contrast and informative band combination of B7, B5, B3 of Landsat-8 was performed (Fig. 9c). This

Table 1
Activity concentrations and radiological health norms for the assessed rocks.

Samples	^{238}U (Bqkg^{-1})	^{232}Th (Bqkg^{-1})	^{40}K (Bqkg^{-1})	^{238}U+^{232}Th+^{40}K	^{232}Th/^{40}K	^{232}Th/^{238}U	D nGy/h	H_{in}	H_{ex}	I_γ	AED_{out} (mSv/y)	AED_{in} (mSv/y)	R_{aeq}	ELCR
UD1	1488.00	707.00	1345.90	2052.90	0.53	0.53	1167.23	11.05	7.03	8.94	1.43	5.73	2602.64	5.01
UD2	1364.00	654.48	1064.20	1718.68	0.61	0.61	1067.10	10.12	6.43	8.17	1.31	5.23	2381.85	4.58
UD3	992.00	610.04	1032.90	1642.94	0.59	0.59	876.23	7.93	5.25	6.70	1.07	4.30	1943.89	3.76
UD4	1054.00	626.20	1408.50	2034.70	0.44	0.44	929.43	8.41	5.56	7.11	1.14	4.56	2057.92	3.99
UD5	1264.80	569.64	970.30	1539.94	0.59	0.59	964.00	9.24	5.82	7.39	1.18	4.73	2154.10	4.14
UD6	979.60	484.80	1001.60	1486.40	0.48	0.48	786.17	7.38	4.73	6.02	0.96	3.86	1749.99	3.37
UD7	855.60	678.72	1095.50	1774.22	0.62	0.62	865.95	7.47	5.16	6.61	1.06	4.25	1910.52	3.72
UD8	719.20	505.00	1001.60	1506.60	0.50	0.50	687.65	6.05	4.10	5.26	0.84	3.37	1518.47	2.95
UD9	1674.00	1999.80	1439.80	3439.60	1.39	1.39	2112.16	17.07	12.54	16.06	2.59	10.36	4644.58	9.07
UD10	1574.80	715.08	1064.20	1779.28	0.67	0.67	1198.10	11.49	7.24	9.18	1.47	5.88	2679.31	5.14
Min.	719.20	484.80	970.30	1486.40	0.44	0.44	687.65	6.05	4.10	5.26	0.84	3.37	1518.47	2.95
Max.	1674.00	1999.80	1439.80	3439.60	1.39	1.39	2112.16	17.07	12.54	16.06	2.59	10.36	4644.58	9.07
Avg.	1196.60	755.08	1142.45	1897.53	0.64	0.64	1065.40	9.62	6.39	8.14	1.31	5.23	2364.33	4.57
SD	323.52	444.32	181.46	577.03	0.27	0.27	401.20	3.13	2.38	3.04	0.49	1.97	880.00	1.72

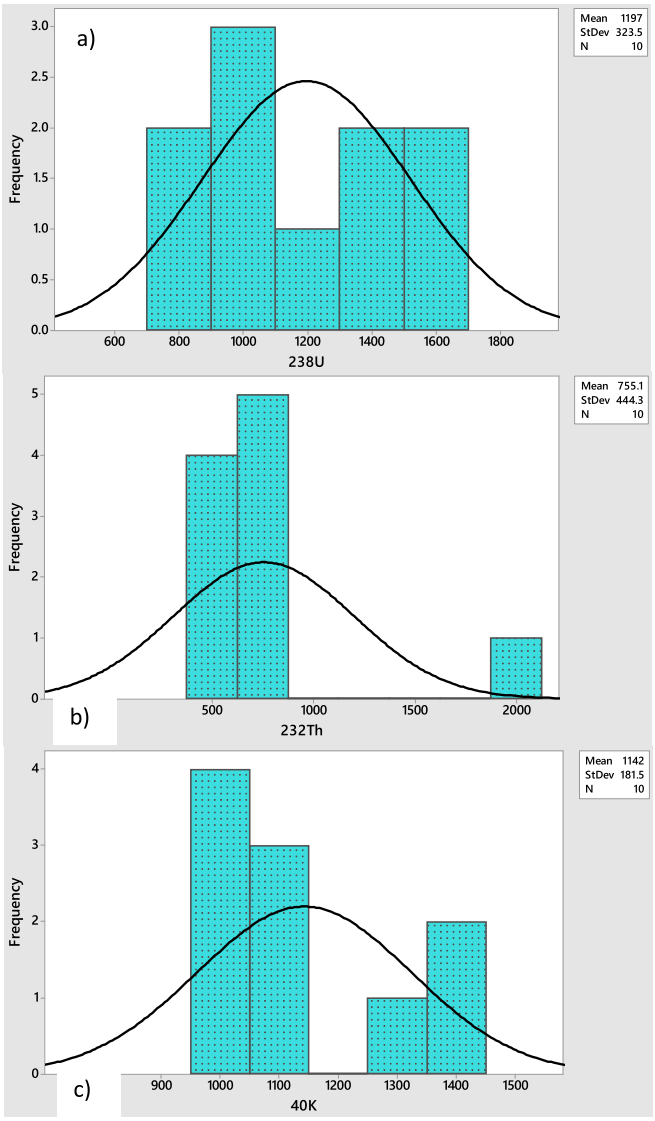

Fig. 5. Frequency distribution of: a) ^{238}U, b) ^{232}Th, and c) ^{40}K.

combination successfully differentiates between the different rock units in the study area. Where the highly foliated metavolcanics appear strike at NW and offer different light and dark colors which represent the heterogeny of moderate to basic metavolcanics. Granitic rocks appear as dark brown pixels. The ring complex of Jabal Mansuri-Um Domi is discriminated fantastically in four components of synogabbro in dark pixels, quartz-syenite in light brown pixels, trachyte in dark green pixels and calcite-brucite in yellowish green pixels (Fig. 9c).

4.4.3. Band ratios (BR)

Several targeted band ratios were generated to enhance specific lithological and mineralogical features: BR of B7/B5 of Sentinal-2 emphasized felsic and altered intrusive rocks such as ring complex (Fig. 9d); BR of B6/B7 of Sentinal-2 highlighted alteration materials (clay/calcite rich areas) in bright pixels (Fig. 9e). Where the BR of B6/B2 of Sentinal-2 enhanced ferruginous, and siliceous zones. The BR ratio of 7/5, 6/7 and 6/2 in RGB of Sentinal-2 discriminates the lithological units in high contrast colors. The metavolcanics appear in reddish green pixels, granitic rocks in reddish orange colors and the four components of the ring complex appear good in their oval shape. Synogabbro enhanced in reddish green, quartz-syenite in red pixels, trachyte in dark green pixels where calcite-brucite in bright green pixels (Fig. 9f). Moreover, three band ratio of Landsat-8 were generated. These ratios

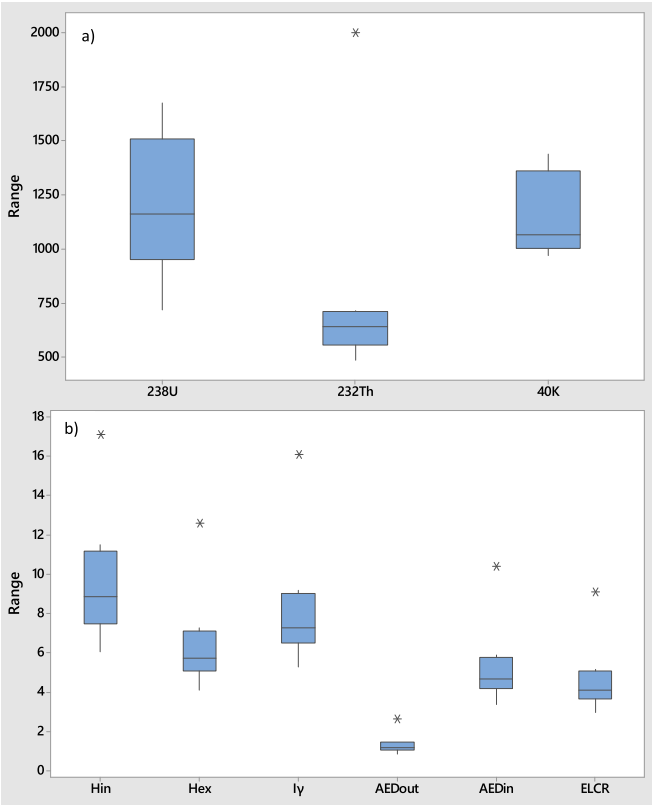

Fig. 6. Box plots for: **a)** ^{40}K, ^{238}U, and ^{232}Th concentrations; and **b)** radiological norms including H_{in}, H_{ex}, I_{γ}, AED_{out}, AED_{in}, and ELCR.

are 6/7–6/2-4/2 in RGB, 6/7–6/5-4/2 in RGB, and 7/5–54/-6/7 in RGB (Fig. 10a, b, and c, respectively). The three band ratios discriminate the lithologic units successfully with sharp contacts and distinctive colors. Especially the four components of the ring complex are separated with bright and colorful pixels.

4.4.4. *Decorrelation stretching (DS)*

To reduce the cross correlation between spectral bands while maintaining the quality of pixel brightness. This technique is used mostly in the areas of heterogeneity and has high spectral similarity between rock units. The combination bands of 7,5,3 of Landsat-8 was selected to decorrelated and its bright and high contrast multi-color image is produced (Fig. 10d). Um Domi ring complex components were successfully separated. The synogabbro attains dark green colo, quartz-syenite attains remarkable purple color, trachyte exhibits olive green, and the altered calcite attains bright green color. This image offered excellent rock units discrimination especially for the Um Domi rock units.

4.4.5. *Principal Component Analysis (PCA)*

The PCA was applied to bands B2, B4, B5, B6, and B7 of sentinel-2. The first three components captured the majority of spectral variance (PC1 ~ 67 %, PC2 ~ 20 %). The PCA-321 in RGB of sentinel-2 (Fig. 10e) and PCA-321 in RGB of Landsat-8 (Fig. 10f) provided enhanced separation between rock units of the Um Domi ring complex and they were particularly effective in defining contact zones and faulted structures.

The PCA results indicate that PC1 explains ~98.8 % of the spectral variance (Table 4), mainly reflecting overall albedo contrasts and effectively distinguishing the granitoid bodies from the surrounding metavolcanic and metasedimentary units. PC2, although accounting for only ~1.1 % of the variance, introduces subtle but critical spectral contrasts that support the discrimination of lithological units with comparable brightness, such as differentiating metavolcanics from

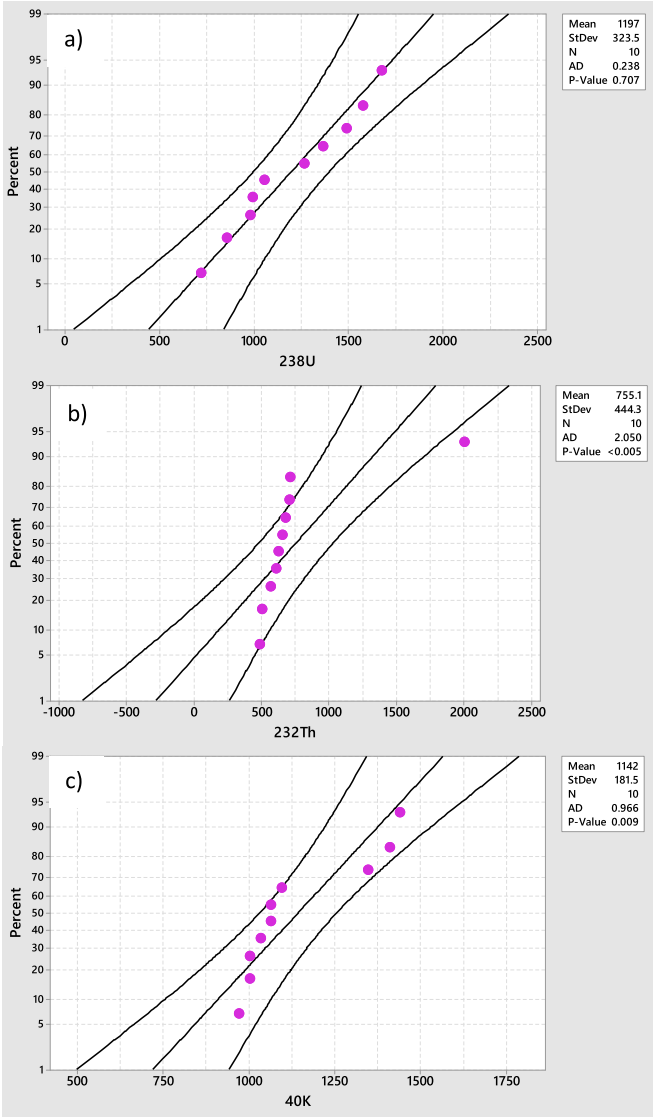

Fig. 7. Distribution probability of: a) ^{238}U, b) ^{232}Th, c) ^{40}K.

metasediments and highlighting alteration zones. The PC1–PC2 scatter plot (Fig. 11a) demonstrates the dominance of PC1 as the main axis of spectral separation, while PC2 refines the clustering and enhances the recognition of lithological variability. To strengthen the PCA outcomes and ensure a more advanced and reproducible analysis, we further integrated the PCA results with an unsupervised KMeans clustering approach. This combined PCA–KMeans workflow produced clear and objective lithological groupings (Fig. 11b), effectively delineating granitoids, metavolcanics, and metasedimentary rocks, and highlighting mineralized or altered zones. This demonstrates the methodological advancement of the Python-based implementation compared to conventional software tools.

4.4.6. *Minimum noise fraction (MNF)*

This technique is one of most effective techniques in lithological discrimination because it decreases and isolates noise data to produce high colorful spectral image (Boardman and Kruse 1994). In this work, the Landsat-8 data was subjected to MNF technique and MNF-432 in RGB has been produced (Fig. 12a). It shows fantastic discrimination of trachyte in orange color, synogabbro in greenish yellow, quartz-syenite in bright green and the altered calcite in bright purple color. Distinctive separation to granite and metavolcanics. Moreover, the incision of the fractures can be observed and detected.

Table 2
Comparison of ^{238}U, ^{40}K, and ^{232}Th concentrations of the Um Domi rocks.

Location	^{238}U (Bqkg^{-1})	^{226}Th (Bqkg^{-1})	^{40}K (Bqkg^{-1})	Reference
Jeddah shoreline	13.14	5.05	139.09	Al-Mur et al. (2025)
Saudi Arabia	28.82	34.83	665.08	AlZahrani et al. (2011)
Spain	84	42	1138	Guillén et al. (2014)
Nigeria, Irepodun	5.42	3.07	735.24	Kanmi et al. (2025)
El Gemal Island	12.49	12.63	325.13	Khaleal et al. (2023)
Serbia	200	77	1280	Kuzmanović et al. (2024)
West coast sediments	2.7–23.5	3.0–31.2	10.7–654.3	Malain et al. (2010)
Yelagiri Hills	19.16	48.56	1146.88	Ravisankar et al. (2015)
Sharm El Luli, Egypt	24.57	23.32	241.83	Saleh et al. (2025b)
Rock materials	25.88	42.82	560.60	Senthilkumar et al. (2014)
Egypt	137.00	82.00	1082.00	Sharaf and Hamideen (2013)
China	356	318	1636	Tuo et al. (2020)
Rize Province	24.5	51.8	334.9	Yuan et al. (1995)
Um Domi area, Egypt	1196.60	755.08	1142.45	The present study

4.4.7. *Image classification*

4.4.7.1. Unsupervised classification. Using the three PCA components as input, a K-Means clustering algorithm (with 4 clusters) was applied. The resulting classified map showed four different rock units which include, metavolcanics, trachyte plugs, and Wadi deposits, (Fig. 12b). It seems that the unsupervised classification offers low accuracy in lithological mapping of the study area and unable to differentiate between the eight rock units in the study area. Therefore, the present study adopted two types of supervised algorithms to make advanced geological mapping to the study area. They will be discussed in the following section.

4.4.7.2. Supervised classification. The cornerstone to produce a supervised classification map is the spectral signature file. The choice of the different classes in this spectral signature file is based on the results of the above-mentioned image processing techniques and the skill of the operator to perform this classification. The present study adopted two algorithms: the maximum likelihood classification (MLC) and the support vector machine (SVM). These two algorithms are widely applied for lithological mapping in arid and semi-arid regions as the Eastern Desert of Egypt. (e.g. (Abd El-Wahed et al., 2023). The high spectral probability is the base of MLC technique to discriminate the different rock units (Scott & Symons, 1971). Where SVM classifying various rock units based on the spatial extent of similar types in the training classes (Vapnik, 2000). The previous geologic maps (at scale 1:250,000) and field work are used as guides in generating spectral signature files. Eight training classes for the different lithological units were in the study area have been delineated. The resultant classified geologic maps of the study area using MLC and SVM, are presented in Fig. 12c and d. The accuracy assessment of the two produced classified maps was performed based on the stratified random sampling method. The overall accuracy of the MLC classified map was 86.06 % with 0.836 Kappa Coefficient but the overall accuracy of SVM classified map was 86.47 % with 0.838 Kappa Coefficient. The two classification algorithms ring complex rock units with high accuracy. The final generated geologic map (Fig. 1) is verified by fieldwork, rock samples, and petrography.

4.5. *Discussion*

4.5.1. *Radioactive minerals and -bearing rocks mapping*

Remotely sensed data has proven to be powerful in detection of the radioactive minerals bearing rocks. The successful detection of the

Table 3
The top five band combinations ranked by OIF of Sentinal-2 band combination.

Rank	Band Combination	OIF Value
1	B5, B6, B7	5061.44
2	B4, B5, B6	4969.77
3	B4, B6, B7	4903.37
4	B4, B5, B7	4689.45
5	B3, B5, B6	4587.73

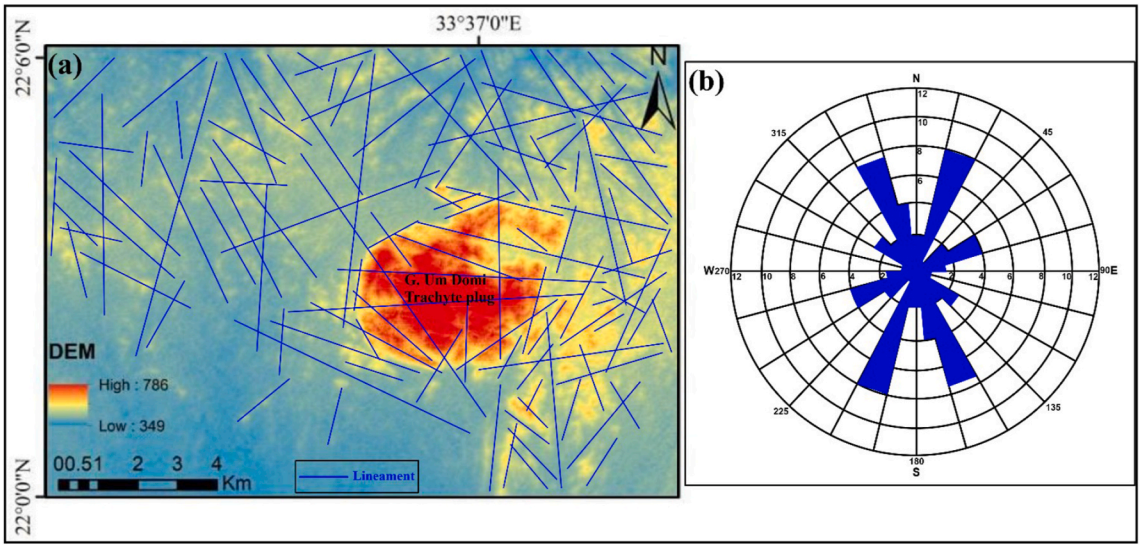

Fig. 8. **a**) Surface structures extracted from the DEM with 30 m spatial resolution; and **b**) Rose diagram displays the major structures trends.

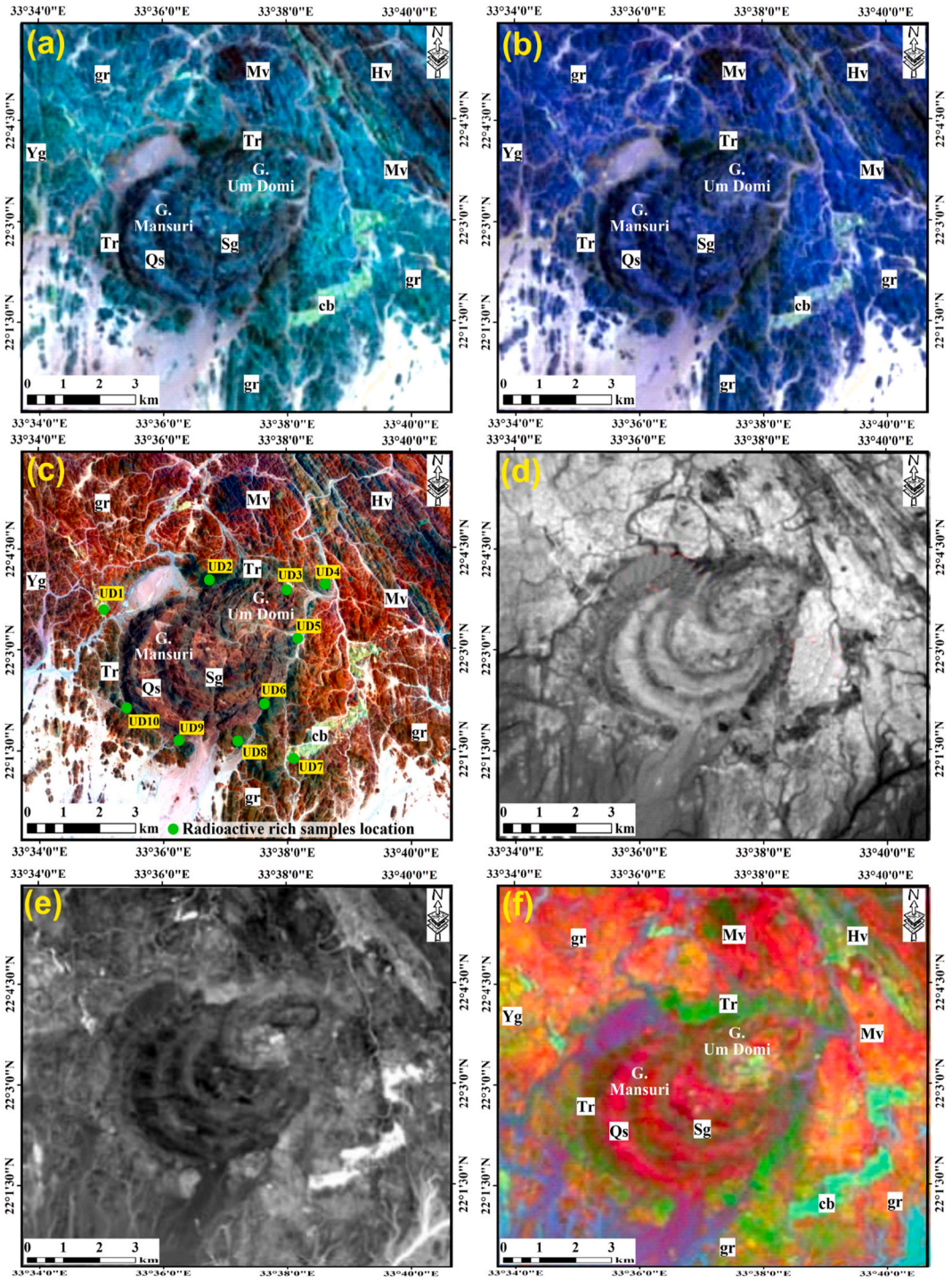

Fig. 9. Band composites of 567 in RGB: a) and 456 in RGB: b) of Sentinal-2 and 753 in RGB of Landsat-8 (c), Band ratio of 7/5; d) and 6/7; e) of Sentinal-2 and f) band ratio of 7/5, 6/7, 6/2 in RGB highlights the rock units in high contrast. Note: the green points on (c) are the geographic location of radioactive rich samples in Table (1). For abbreviations, please see Fig. (1).

alteration minerals such as illite, chlorite, kaolinite, hematite and sericite is the important clues in identifying the zone of radioactive mineralization and hydrothermal alterations (Ahmed et al., 2025; El-Qassas et al., 2023). Therefore, the abundance of the alteration minerals ex. clay, kaolinite, illite, and chlorite provides a great indicator for the uranium mineralization zones. The present study adopted the band ratio of B6/B7 of Landsat-8 (Fig. 13a) to detect clay and OH-bearing minerals and B4/B2 of Landsat-8 (Fig. 13b) to detect the Fe minerals. The two ratios are widely used and effectively detect the alteration zones. The high abundance of the alteration minerals is presented as bright pixels in the grey scale images, but we prefer to offer it here by pseudo color to enhance the high abundance of the target mineral (s) by the red color. Figure 13a shows that the clay and OH-bearing minerals are concentrated over granitic rocks, trachyte, calcite-brucite and around J. Um Domi. Whereas the altered products of Fe minerals are distributed around the Um Domi ring complex (Fig. 13b). Importantly, it is noticed that the radioactive rich samples are located in the zone of moderate to high concentration of clay and Fe

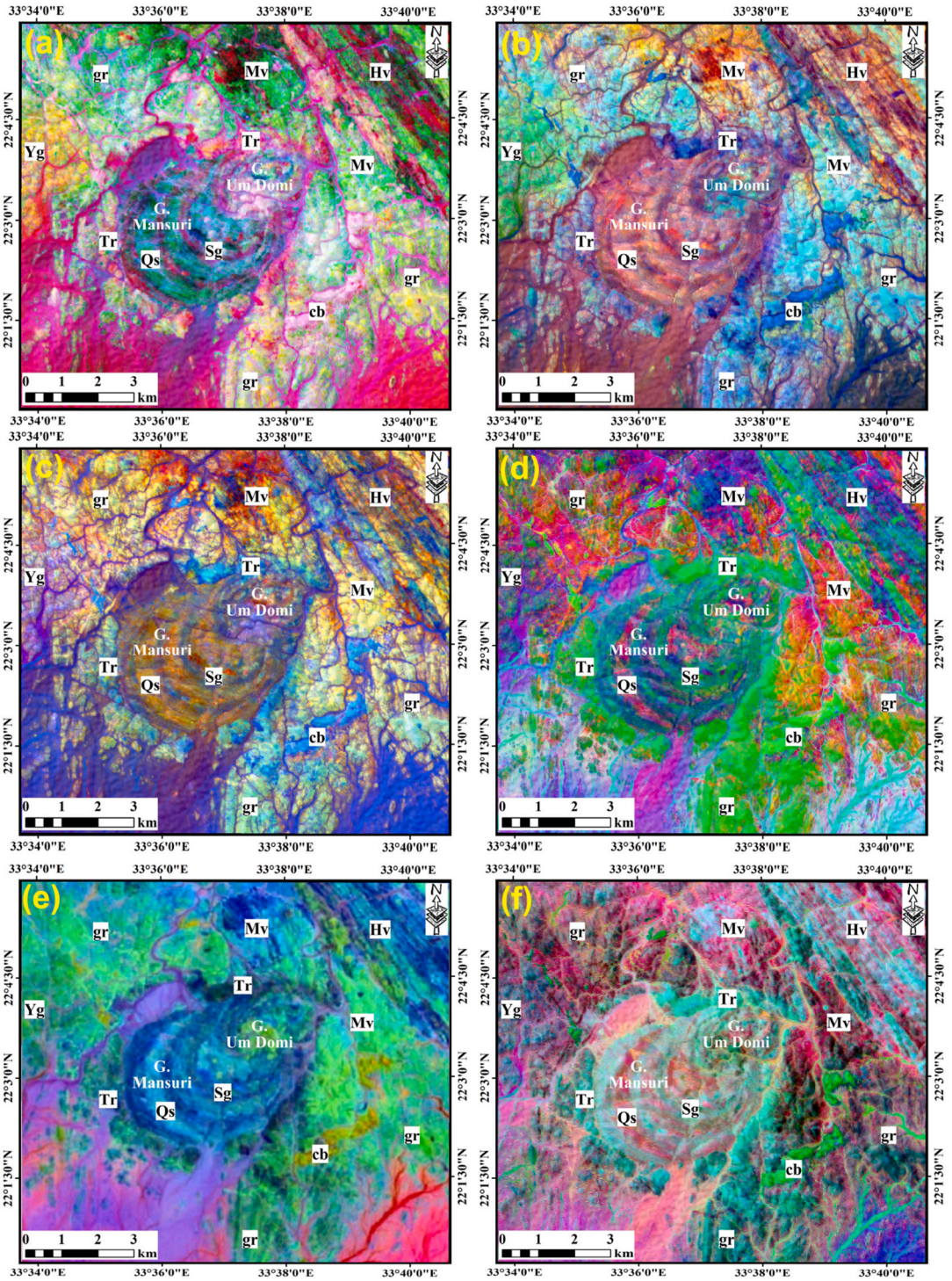

Fig. 10. Landsat-8 band ratios of 6/7–6/2-4/2 in RGB: a), 6/7–6/5-4/2 in RGB; b), and 7/5–54/-6/7 in RGB; c-d) Decorrelation stretching of bands 753 of Landsat-8, PCA-321 of Sentinal-2; e) and Landsat-8 (f). For abbreviations, please see Fig. (1).

Table 4
Explained variance ratio of the first three principal components derived from Sentinel-2 bands.

Principal Component	Explained Variance Ratio
PC1	0.988052
PC2	0.01096
PC3	0.000443

minerals (Fig. 13a and b).

Structurally, Um Domi is located at the end of the active shear zone of Allaqi-Heini. The detected structural features (normal faults and strike slip faults) are trending mostly in NW-SE, NE-SW, E-W and N-S (Figs. 1 and 13c). The complexity of the structural setting of the study area reflects that it was subjected to successive tectonic events from Precambrian to recent. Fractures and faults play as pathways for the radioactive bearing solution and mineralization. Um Domi ring complex is dissected by the dextral strike slip faults (Figs. 1 and 13c). In Egypt many authors (ex. (Sherif, 1997) recorded high radiometric anomalies

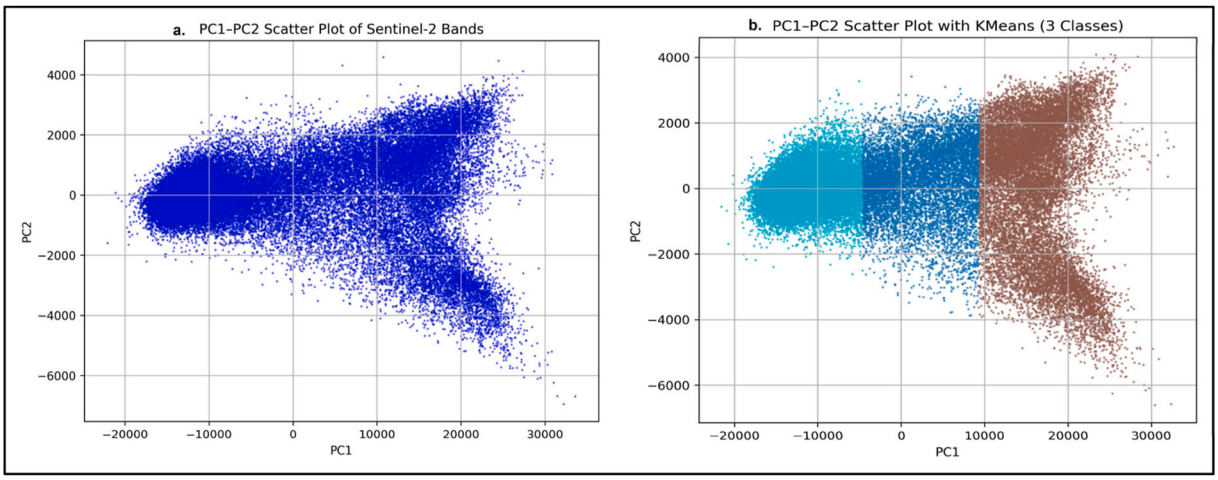

Fig. 11. PC1–PC2 of Sentinal-2 scatter plots: (a) pixel distribution showing PC1 dominance with minor contribution from PC2; (b) integration with K-Means clustering highlighting distinct lithological groups.

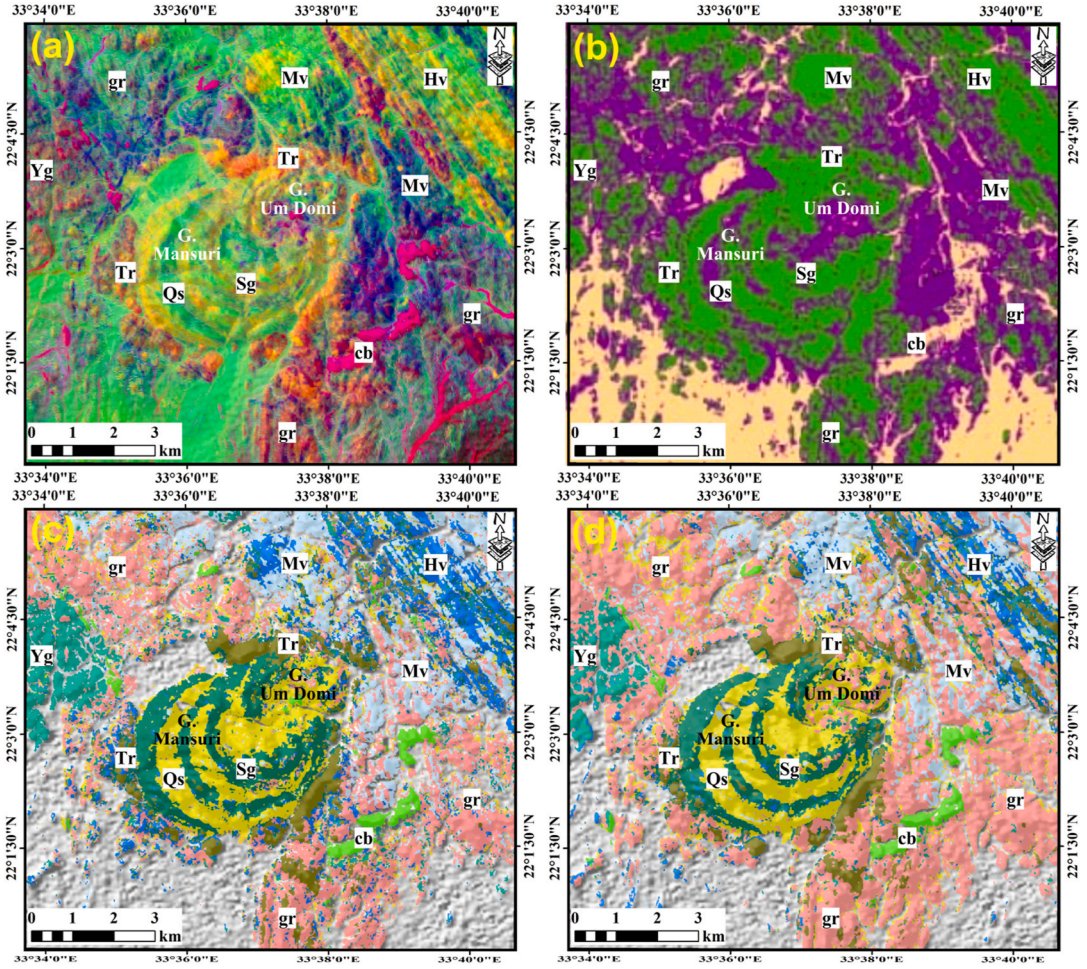

Fig. 12. a) The MNF-432 in RGB of Landsat-8; **b**) The classified map using unsupervised algorithms; **c**) the classified maps using MLC**; and d**) the classified map using SVM algorithm.

along NE-SW and NW–SE directions (Rabie & Ammer, 1988). considered NE-SW faults as an important trend for high radiometric anomalies.

To enhance the role of geology, structure and alteration in concentration of the radioactive mineralization. A geospatial model was produced by integrating potential source rock (ring complex), high alteration zones (clay and Fe minerals), lineament density, major faults, and rock samples containing radioactive mineralization (Fig. 13c). This figure 13c shows that the ring complex and alteration zones are structurally controlled. The measured rock samples containing high radiation level fall into the high lineament density areas, into moderate to high abundance alteration zones and along with major faults. Consequently, lithology, alteration and structural controls play an important role in the

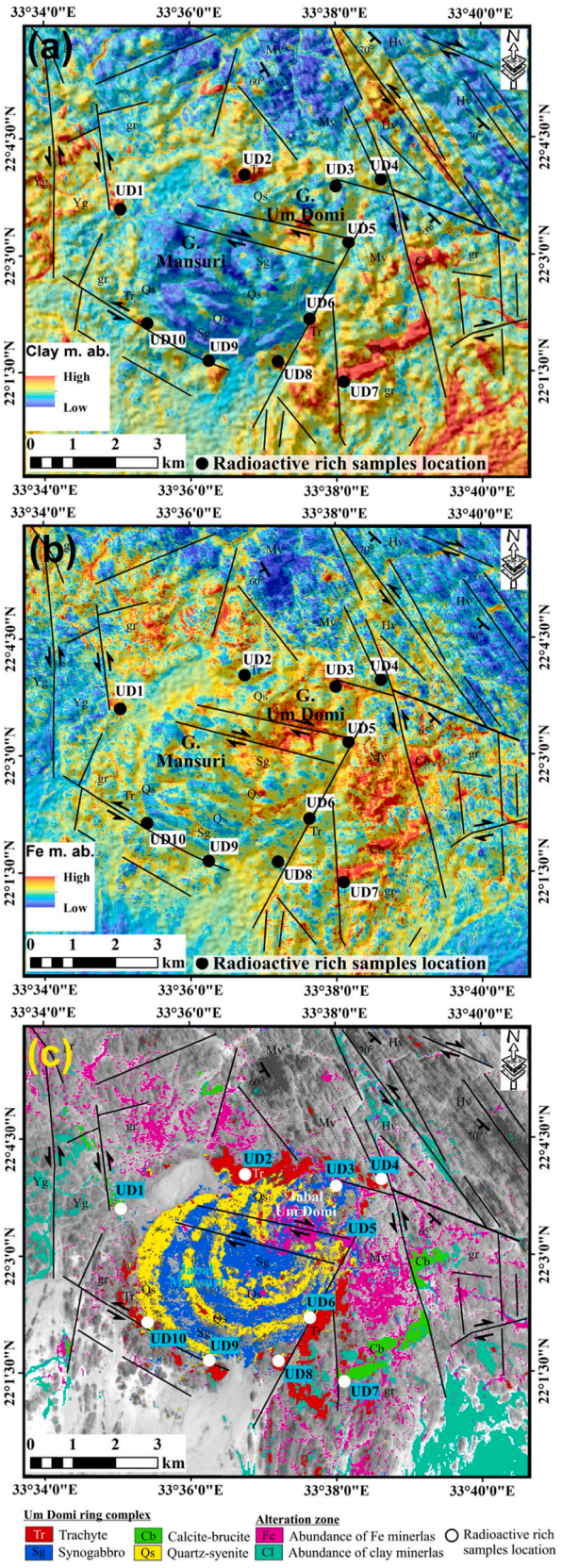

Fig. 13. a) Abundance of altered clay minerals; **b)** Abundance of the ferruginous materials; and **c)** model integrating the main factors affecting radioactive mineralization.

distribution of radioactive mineralization in the study area.

4.5.2. *Radiation risk impact*

The radioactivity of Um Domi trachyte has been evaluated using a range of metrics, including the D, H_{ex}, H_{in}, AED $_{out\ \&\ in}$, ELCR, R_{aeq}, and Iγ (Table 1).

Box plot of the radiological norms (H_{ex}, H_{in}, AED $_{out\ \&\ in}$, ELCR, and Iγ) for the assessed trachyte samples reveals that the H_{ex} exhibit a wide variation relative to other parameters. There is one sample (no UD9) plot outliers for all the radiological norms due to high content of ^{232}Th ^{238}U, and ^{40}K (Fig. 6).

As noted by Kumar et al. (2024) and UNSCEAR (2000), the D index is a crucial metric for assessing the strength of terrestrial gamma radiation at elevations above 1 m. The D values of the examined samples ranged from 687.65 to 2112.16 nGyh^{-1}. Their marked radiation impact was highlighted by their highly higher D values, which are exceeding the UNSCEAR (2010) acknowledged worldwide acceptable level of 59 nGyh^{-1} (Table 1).

A common tool for evaluating possible threats to human health is the H_{in} and H_{ex} hazard factors. The predicted mean H_{ex} and H_{in} results for the rocks under examination are 6.39 ± 2.38 and 9.62 ± 3.13, respectively, which are exceeding the globally advised safety level and indicate serious radiological hazards (Attallah et al., 2018; European Commission, 1999; Shahrokhi et al., 2020; Wais et al., 2023; Özden et al., 2023).

The yearly dose effective for both outdoor (AED_{out}) and indoor (AED_{in}) exposure conditions was estimated using the D findings, a dose conversion factor of 0.7 SvGy^{-1}, and occupancy coefficients of 0.2 for outdoor and 0.8 for interior conditions. The average AED_{out} values of the rocks under examination were 1.31 ± 0.49 mSvy^{-1}, which is higher than the globally advised level (UNSCEAR, 2010). Comparing the assed rocks' AEDin readings (av. 5.23 ± 1.97 mSvy^{-1}) to the globally advised level reveals a similar pattern (O'Brien & Sanna, 1976; UNSCEAR, 2000).

With an average Iγ value of 8.14 ± 3.04, the assessed rocks are over the globally advised level of unity (Qureshi et al., 2014). Therefore, exposure to gamma-rays affects both inner and outer alpha releases as well as the Raeq. The estimated mean Raeq values for the assed rocks show a mean of 2364.33 ± 880 Bqkg^{-1}, which is significantly higher than the globally acceptable values listed by (Hanfi et al., 2022; UNSCEAR, 2010), which range from 1518.47 to 4644.58 Bqkg^{-1}.

The evaluated rocks' expected ELCR values are 4.57 ± 1.72 × 10^{-3}, which is much higher than the permitted level. According to these results, those who are exposed to Um Domi trachyte for an extended length of time through intimate contact may be at higher risk of developing cancer (O'Brien & Sanna, 1976; Qureshi et al., 2014; UNSCEAR, 2000).

The degree of cooperation between the radioactive components is determined by the Pearson correlation of radioactive metrics in the Um Domi trachyte rocks, which is displayed in Table 5. According to Tanasković et al. (2012), the correlation frequency was separated into four groups: weak (0.00–0.19), moderate (0.2–0.39), high (0.4–0.79), and very strong (0.8–1.0). Table 5 demonstrates a strong positive correlation (R2 = 0.609 & 0.46), between ^{238}U and ^{232}Th & ^{40}K, respectively. This table shows that, in comparison to ^{232}Th, there is a moderate link between ^{238}U and ^{40}K activity. The simultaneous presence of these radionuclides in nature explains this (A. M. A. Adam & Eltayeb, 2012). Additionally, there is a significant and positive correlation between the ^{238}U and ^{232}Th and the radiological risk indicators. This is because radiological factors are linked to radionuclides, which are known to be primarily gamma-ray generating elements in nature.

5. Conclusions

By integrating field observations and laboratory results, the study's main goal is to create an accurate lithological map that can aid future mineral development initiatives. On top of that, using a NaI detector, the natural radioactivity levels of volcanic rocks from Um Domi were

Table 5
Pearson's correlation of the activity concentrations and hazard parameters.

	^{238}U	^{232}Th	^{40}K	H_{in}	H_{ex}	Iγ	AED_{out}	AED_{in}	R_{aeq}
^{232}Th	0.609								
^{40}K	0.464	0.636							
H_{in}	0.898	0.896	0.620						
H_{ex}	0.815	0.956	0.646	0.987					
Iγ	0.808	0.959	0.649	0.985	1.000				
AED_{out}	0.806	0.960	0.650	0.984	1.000	1.000			
AED_{in}	0.805	0.961	0.649	0.984	1.000	1.000	1.000		
R_{aeq}	0.815	0.956	0.646	0.987	1.000	1.000	1.000	1.000	
ELCR	0.804	0.961	0.649	0.984	1.000	1.000	1.000	1.000	1.000

investigated. Since zircon, uranothorite, and kasolite are examples of radioactive accessory minerals that have radionuclides in their crystal structure, the activity concentrations that were obtained are higher than the internationally advised standards. The results of a number of radioactive risk indicators that were used to evaluate possible health risks are superior to international safety requirements. This is implying that the increased natural gamma radiation linked to these rocks may constitute a serious health danger, owing to their radioactive material concentration. Multiple remote sensing approaches, including DEM, OIF analysis, PCA, MNF and unsupervised/supervised classification methods have been utilized to facilitate the discrimination of lithological units within the study area. Consequently, lithology, alteration and structural controls play an important role in the distribution of radioactive mineralization in the study area. It's noticed that the measured rock samples containing high radiation level fall into the high lineament density areas, into moderate to high abundance alteration zones and along with major faults.

CRediT authorship contribution statement

El Saeed R. Lasheen: Writing – review & editing, Writing – original draft, Supervision, Software, Resources, Investigation, Data curation, Conceptualization. **Basma A. El-Badry:** Writing – review & editing, Visualization, Resources, Funding acquisition. **Samir Z. Kamh:** Writing – review & editing, Writing – original draft, Software, Conceptualization. **Mabrouk Sami:** Writing – review & editing, Formal analysis, Software. **Naglaa AbdelAll:** Writing – review & editing, Data curation, Investigation, Software. **Ioan V. Sanislav:** Writing – review & editing, Project administration, Data curation, Supervision. **Samia S. Hasan:** Writing – review & editing, Software. **Gehad M. Saleh:** Writing – review & editing, Supervision, Methodology, Formal analysis, Conceptualization.

Availability of data and material

This article contains all of the data examined during this investigation.

Ethical approval

No research with human beings has been carried out by any of the authors of this paper.

Funding

This work was supported and funded by the Deanship of Scientific Research at Imam Mohammad Ibn Saud Islamic University (IMSIU) (grant number IMSIU-DDRSP2502).

Conflict of interest

None.

References

Abd El-Wahed, M., Kamh, S., Abu Anbar, M., Zoheir, B., Hamdy, M., Abdeldayem, A., Lebda, E. M., & Attia, M. (2023). Multisensor satellite data and field studies for unravelling the structural evolution and gold metallogeny of the Gerf ophiolitic Nappe, Eastern desert, Egypt. *Remote Sensing, 15*(8), 1974. https://doi.org/10.3390/rs15081974

Abdel-Aal, M. M., Tawfik, F. S., & Kandil, N. M. (2024). Radiation dose assessments for generic nuclear power plants part I: Routine operation. *Applied Radiation and Isotopes, 211*, Article 111412. https://doi.org/10.1016/j.apradiso.2024.111412

Abdul Sani, S. F., Muhamad Azim, M. K., Marzuki, A. A., Khandaker, M. U., Almugren, K. S., Daar, E., Alkallas, F. H., & Bradley, D. A. (2022). Radioactivity and elemental concentrations of natural and commercial salt. *Radiation Physics and Chemistry, 190*, Article 109790. https://doi.org/10.1016/j.radphyschem.2021.109790

Acker, J., Leptoukh, G., Shen, S., Zhu, T., & Kempler, S. (2008). Remotely-sensed chlorophyll a observations of the northern Red Sea indicate seasonal variability and influence of coastal reefs. *Journal of Marine Systems, 69*(3–4), 191–204. https://doi.org/10.1016/j.jmarsys.2005.12.006

Adam, A. M. A., & Eltayeb, M. A. H. (2012). Multivariate statistical analysis of radioactive variables in two phosphate ores from Sudan. *Journal of Environmental Radioactivity, 107*, 23–43. https://doi.org/10.1016/j.jenvrad.2011.11.021

Adam, M. M. A., Lv, X., Fathy, D., Abdel Rahman, A. R. A., Ali, A. A., Mohammed, A. S., Farahat, E. S., & Sami, M. (2022). Petrogenesis and tectonic implications of Tonian island arc volcanic rocks from the Gabgaba Terrane in the Arabian-Nubian Shield (NE Sudan). *Journal of Asian Earth Sciences, 223*, Article 105006. https://doi.org/10.1016/j.jseaes.2021.105006

Ahmed, S. B., Elhusseiny, A. A., Azzazy, A. A., & El-Qassas, R. A. Y. (2025). Utilization of airborne geophysical data and remote sensing to identify radioactive and hydrothermal alteration zones in the East Qena area, Central Eastern Desert, Egypt. *Acta Geophysica*. https://doi.org/10.1007/s11600-025-01652-z

Akkurt, I., & Günoğlu, K. (2014). Natural radioactivity measurements and radiation dose estimation in some sedimentary rock samples in Turkey. *Science and Technology of Nuclear Installations*, 1–6. https://doi.org/10.1155/2014/950978, 2014.

Al-Hamarneh, I. F., & Awadallah, M. I. (2009). Soil radioactivity levels and radiation hazard assessment in the highlands of northern Jordan. *Radiation Measurements, 44*(1), 102–110. https://doi.org/10.1016/j.radmeas.2008.11.005

Al-Mur, B. A., Aljahdali, M. H., Almeelbi, T., & Lasheen, E. S. R. (2025). Spatial radionuclide distribution, mineralogy, and radiological evaluation of the Jeddah shoreline sediments, Red Sea, Saudi Arabia. *Environmental Monitoring and Assessment, 197*(5), 593. https://doi.org/10.1007/s10661-025-13986-8

Al-Trabulsy, H. A., Khater, A. E. M., & Habbani, F. I. (2011). Radioactivity levels and radiological hazard indices at the Saudi coastline of the Gulf of Aqaba. *Radiation Physics and Chemistry, 80*(3), 343–348. https://doi.org/10.1016/j.radphyschem.2010.09.002

AlZahrani, J. H., Alharbi, W. R., & Abbady, A. G. E. (2011). Radiological impacts of natural radioactivity and heat generation by radioactive decay of phosphorite deposits from northwestern Saudi Arabia. *Australian Journal of Basic and Applied Sciences, 5*(6), 683–690.

Attallah, M. F., Hilal, M. A., & Mohamed, Y. T. (2018). Preliminary investigations on reducing the high radiation risk level of TENORM scale waste from petroleum industry. *Radiochimica Acta, 106*(9), 793–800. https://doi.org/10.1515/ract-2017-2904

Chen, C., Judge, J., & Hulse, D. (2022). PyLUSAT: An open-source Python toolkit for GIS-based land use suitability analysis. *Environmental Modelling & Software, 151*, Article 105362. https://doi.org/10.1016/j.envsoft.2022.105362

Davidson, J. P., & Wilson, I. R. (1989). Evolution of an alkali basalt—Trachyte suite from Jebel Marra volcano, Sudan, through assimilation and fractional crystallization. *Earth and Planetary Science Letters, 95*(1–2), 141–160. https://doi.org/10.1016/0012-821x(89)90173-8

Deer, W. A., Howie, R. A., & Zussman, J. (1992). *An introduction to the rock forming minerals. Second edition. London: Longman Scientific and Technical*.

EGSMA, G. S. OF E.. (1996). *Geologic map of Wadi Jabjabah Quadrangle. Scale*, 1:250000, Cairo, Egypt.

El-Qassas, R. A. Y., Abu-Donia, A. M., & Omar, A. E. A. (2023). Delineation of hydrothermal alteration zones associated with mineral deposits, using remote sensing and airborne geophysics data. A case study: El-bakriya area, Central Eastern Desert, Egypt. *Acta Geodaetica et Geophysica, 58*(1), 71–107. https://doi.org/10.1007/s40328-023-00405-y

European Commission. (1999). *Radiological protection principles concerning the natural radioactivity of building materials. Radiation Protection, 112. Directorate General Environment*. Nuclear Safety and Civil Protection, European Commission.

Farahbakhsh, E., Goel, D., Pimparkar, D., Müller, R. D., & Chandra, R. (2025). Convolutional neural networks for mineral prospecting through alteration mapping with remote sensing data. *PFG – Journal of Photogrammetry, Remote Sensing and Geoinformation Science*. https://doi.org/10.1007/s41064-025-00344-z

Gorelick, N., Hancher, M., Dixon, M., Ilyushchenko, S., Thau, D., & Moore, R. (2017). Google Earth engine: Planetary-scale geospatial analysis for everyone. *Remote Sensing of Environment, 202*, 18–27. https://doi.org/10.1016/j.rse.2017.06.031

Gourgaud, A., & Maury, R. C. (1984). Magma mixing in alkaline series: An example from Sancy volcano (Mont-Dore, Massif Central, France). *Bulletin Volcanologique, 47*(4), 827–847. https://doi.org/10.1007/bf01952346

Guillén, J., Tejado, J. J., Baeza, A., Salas, A., & Muñoz-Muñoz, J. G. (2014). Environmental impact of a granite processing factory as source of naturally occurring radionuclides. *Applied Geochemistry, 47*, 122–129. https://doi.org/10.1016/j.apgeochem.2014.06.001

Gupta, R. P. (2003). Spectra of minerals and rocks. In R. P. Gupta (Ed.), *Remote sensing geology* (pp. 33–52). Springer Berlin Heidelberg. https://doi.org/10.1007/978-3-662-05283-9_3.

Hamdani, N., & Baali, A. (2019). Fracture network mapping using landsat 8 OLI data and linkage with the karst system: A case study of the Moroccan central middle Atlas. *Remote Sensing in Earth Systems Sciences, 2*(1), 1–17. https://doi.org/10.1007/s41976-019-0011-y

Hanfi, M. Y., Abdel Gawad, A. E., Eliwa, H., Ali, K., Taki, M. M., Sayyed, M. I., Khandaker, M. U., & Bradley, D. A. (2022). Assessment of radioactivity in Granitoids at Nikeiba, Southeastern desert, Egypt; radionuclides concentrations and radiological hazard parameters. *Radiation Physics and Chemistry, 200*, Article 110113. https://doi.org/10.1016/j.radphyschem.2022.110113

Jensen, J. R. (2005). *Introductory digital image processing: A remote sensing perspective. 3rd edition. Upper Saddle River: Prentice Hall*.

Kanmi, A. S., Ibrahim, U., Goki, N. G., Rilwan, U., Sayyed, M. I., Maghrbi, Y., Namq, B. F., Najam, L. A., & Wais, T. Y. (2025). Assessment of natural radioactivity and its radiological risks in the soil of local government areas (Asa, Ilorin East, Ilorin South, Irepodun, Moro, and Oyun) in Kwara State, Nigeria. *Case Studies in Chemical and Environmental Engineering, 11*, Article 101040. https://doi.org/10.1016/j.cscee.2024.101040

Kasperek, D., & Podpora, M. (2024). Optimizing geospatial data for ML/CV applications: A python-based approach to streamlining map processing by removing irrelevant areas. *Applied Sciences, 14*(24), Article 11978. https://doi.org/10.3390/app142411978

Khaleal, F. M., Lentz, D. R., Kamh, S. Z., Saleh, G. M., Abdalla, F., & Lasheen, E. S. R. (2024). Remote sensing analysis and geodynamic setting of magmatic spessartine-almandine-bearing leucogranites, Um Addebaa area, southeastern Desert, Egypt: Bulk rock and mineral chemistry. *Physics and Chemistry of the Earth, Parts A/B/C, 136*, Article 103749. https://doi.org/10.1016/j.pce.2024.103749

Khaleal, F. M., Tahoon, M. A., Saleh, G. M., Kamar, M. S., Zakaly, H. M. H., Zidan, I. H., Al-Mur, B. A., Alarif, S. S., & Lasheen, E. S. R. (2023). Dolphin-shaped island: Exploring the natural resources and radiological hazards of Wadi El Gemal Island. *Marine Pollution Bulletin, 194*, Article 115367. https://doi.org/10.1016/j.marpolbul.2023.115367

Khandaker, M. U., Mahmud, A., Siraz, M. M. M., Alam, M. S., Trishna, J. M., Rashid, M. B., Hussin, F., Kassim, M. A., & Osman, H. (2025). Identification of elevated level background radiation areas, exposure scenarios and implications for public health and environmental safety in Malaysia: A comprehensive study. *Radiation Physics and Chemistry, 235*, Article 112851. https://doi.org/10.1016/j.radphyschem.2025.112851

Krebs, M. Y., Pearson, D. G., Fagan, A. J., Bussweiler, Y., & Sarkar, C. (2019). The application of trace elements and Sr–Pb isotopes to dating and tracing ruby formation: The Aappaluttoq deposit, SW Greenland. *Chemical Geology, 523*, 42–58. https://doi.org/10.1016/j.chemgeo.2019.05.035

Kumar, N., Khyalia, B., Yadav, J., Singh, B., Gupta, V., Singh, P. P., Singh, H., & Dalal, R. (2024). Assessment of natural radioactivity in soil around Khetri copper belt of Rajasthan, India. *Journal of Radioanalytical and Nuclear Chemistry, 333*(6), 3185–3194. https://doi.org/10.1007/s10967-023-09301-9

Kuzmanović, P., Filipović Petrović, L., Petrović, J., Forkapić, S., Hansman, J., Velimirović, D., & Knežević Radić, J. (2024). Physico-chemical, technological and radiological characteristics of kaolinized granite from northwestern Serbia. *Radiation Physics and Chemistry, 222*, Article 111885. https://doi.org/10.1016/j.radphyschem.2024.111885

Lasheen, E. S. R., El-Badry, B. A., Mohamed, W. H., Khouqeer, G. A., Sanislav, I. V., & Sami, M. (2025). Radioactivity and aeromagnetic of magmatic suites, Arabian Nubian shield: Petrological and health risk characteristics. *Journal of Radiation Research and Applied Sciences, 18*(4), Article 101910. https://doi.org/10.1016/j.jrras.2025.101910

Lasheen, E. S. R., Sami, M., Hegazy, A. A., Arman, H., Sanislav, I. V., Ahmed, M. S., & Rashwan, M. A. (2024). Petrological characteristics and physico-mechanical properties of dokhan volcanics for decorative stones and building material applications. *Buildings, 14*(11), 3418. https://doi.org/10.3390/buildings14113418

Li, H., Wang, Q., Zhang, C., Su, W., Ma, Y., Zhong, Q., Xiao, E., Xia, F., Zheng, G., & Xiao, T. (2024). Geochemical distribution and environmental risks of radionuclides in soils and sediments runoff of a uranium mining area in south China. *Toxics, 12*(1), 95. https://doi.org/10.3390/toxics12010095

Maithani, P. B., & Srinivasan, S. (2011). Felsic volcanic rocks, a potential source of uranium—An Indian overview. *Energy Procedia, 7*, 163–168. https://doi.org/10.1016/j.egypro.2011.06.022

Malain, D., Regan, P. H., Bradley, D. A., Matthews, M., Santawamaitre, T., & Al-Sulaiti, H. A. (2010). Measurements of NORM in beach sand samples along the Andaman coast of Thailand after the 2004 tsunami. *Nuclear Instruments and Methods in Physics Research Section A: Accelerators, Spectrometers, Detectors and Associated Equipment, 619*(1–3), 441–445. https://doi.org/10.1016/j.nima.2009.11.047

Masoumi, F., Eslamkish, T., Abkar, A. A., Honarmand, M., & Harris, J. R. (2017). Integration of spectral, thermal, and textural features of ASTER data using random forests classification for lithological mapping. *Journal of African Earth Sciences, 129*, 445–457. https://doi.org/10.1016/j.jafrearsci.2017.01.028

Nafigin, I. O., Ishmukhametova, V. T., Ustinov, S. A., Minaev, V. A., & Petrov, V. A. (2022). Geological and mineralogical mapping based on statistical methods of remote sensing data processing of Landsat-8: A case study in the Southeastern transbaikalia, Russia. *Sustainability, 14*(15), 9242. https://doi.org/10.3390/su14159242

O'Brien, K., & Sanna, R. (1976). The distribution of absorbed dose-rates in humans from exposure to environmental gamma rays. *Health Physics, 30*.

Özden, S., & Aközcan, S. (2021). Natural radioactivity measurements and evaluation of radiological hazards in sediment of Aliağa Bay, İzmir (Turkey). *Arabian Journal of Geosciences, 14*(1), 64. https://doi.org/10.1007/s12517-020-06446-9

Özden, S., Pehlivanoğlu, S. A., & Günay, O. (2023). Evaluation of natural radioactivity in soils of Konya (Turkey) and estimation of radiological health hazards. *Environmental Monitoring and Assessment, 195*(12), 1523. https://doi.org/10.1007/s10661-023-12162-0

Pavlidou, S., Koroneos, A., Papastefanou, C., Christofides, G., Stoulos, S., & Vavelides, M. (2006). Natural radioactivity of granites used as building materials. *Journal of Environmental Radioactivity, 89*(1), 48–60. https://doi.org/10.1016/j.jenvrad.2006.03.005

Pour, A. B., & Hashim, M. (2012). The application of ASTER remote sensing data to porphyry copper and epithermal gold deposits. *Ore Geology Reviews, 44*, 1–9. https://doi.org/10.1016/j.oregeorev.2011.09.009

Pour, A., Park, Y., Crispini, L., Läufer, A., Kuk Hong, J., Park, T.-Y. S., Zoheir, B., Pradhan, B., Muslim, A. M., Hossain, M. S., & Rahmani, O. (2019). Mapping listvenite occurrences in the damage zones of Northern Victoria land, Antarctica using ASTER satellite remote sensing data. *Remote Sensing, 11*(12), 1408. https://doi.org/10.3390/rs11121408

Pour, A. B., Park, T.-Y., Park, Y., Hong, J., Zoheir, B., Pradhan, B., Ayoobi, I., & Hashim, M. (2018). Application of multi-sensor satellite data for exploration of Zn–Pb sulfide mineralization in the franklinian Basin, North Greenland. *Remote Sensing, 10*(8), 1186. https://doi.org/10.3390/rs10081186

Qureshi, A. A., Tariq, S., Din, K. U., Manzoor, S., Calligaris, C., & Waheed, A. (2014). Evaluation of excessive lifetime cancer risk due to natural radioactivity in the rivers sediments of Northern Pakistan. *Journal of Radiation Research and Applied Sciences, 7*(4), 438–447. https://doi.org/10.1016/j.jrras.2014.07.008

Rabie, S. I., & Ammer, A. A. (1988). Maximum principal stress and tectonic trends as revealed from aeromagnetic and aeroradiometric data, Gabal Maghrabia area, Eastern Desert, Egypt. *The Journal of Geology, 32*, 91–129.

Raghavendra, T., Vishwaprasad, K., Kalyani, G., Vijayalakshmi, T., Himabindu, V., Arunachalam, J., Padmasavithri, P., Kumar, V., & Tripathi, R. M. (2019). Assessment of natural radioactivity in soils around the proposed uranium mining site of lambapur – Peddagattu and seripally, India. *Journal of the Geological Society of India, 93*(2), 223–227. https://doi.org/10.1007/s12594-019-1156-2

Ramola, R. C., Choubey, V. M., Prasad, G., Gusain, G. S., Tosheva, Z., & Kies, A. (2011). Radionuclide analysisin the soil of Kumaun Himalaya, India, using gamma ray spectrometry. *Current Science, 100*(6), 6–25.

Rashwan, M. A., Lasheen, E. S. R., & Azer, M. K. (2023). Thermal and physico-mechanical evaluation of some magmatic rocks at Homrit Waggat area, Eastern Desert, Egypt: Petrography and geochemistry. *Bulletin of Engineering Geology and the Environment, 82*(6), 199. https://doi.org/10.1007/s10064-023-03208-1

Ravisankar, R., Chandramohan, J., Chandrasekaran, A., Prince Prakash Jebakumar, J., Vijayalakshmi, I., Vijayagopal, P., & Venkatraman, B. (2015). Assessments of radioactivity concentration of natural radionuclides and radiological hazard indices in sediment samples from the East Coast of Tamilnadu, India with statistical approach. *Marine Pollution Bulletin, 97*(1–2), 419–430. https://doi.org/10.1016/j.marpolbul.2015.05.058

Sabins, F. F. (1999). Remote sensing for mineral exploration. *Ore Geology Reviews, 14*(3–4), 157–183. https://doi.org/10.1016/S0169-1368(99)00007-4

Sadek, M. F., El-kalioubi, B. A., Ali-Bik, M. W., El Hefnawi, M. A., & Elnazer, A. A. (2020). Utilizing Landsat-8 and ASTER data in geologic mapping of hyper-arid mountainous region: Case of Gabal Batoga area, South Eastern Desert of Egypt. *Environmental Earth Sciences, 79*(5), 101. https://doi.org/10.1007/s12665-020-8845-4

Sahoo, S. K., Hosoda, M., Kamagata, S., Sorimachi, A., Ishikawa, T., Tokonami, S., & Uchida, S. (2011). Thorium, uranium and rare Earth elements concentration in weathered Japanese soil samples. *Progress in Nuclear Science and Technology, 1*(0), 416–419. https://doi.org/10.15669/pnst.1.416

Saleh, G. M., Kamar, M. S., Khaleal, F. M., Azer, M. K., Nasr, T., & Lasheen, E. S. R. (2025). Petrogenesis and tectonic evolution of tourmaline- bearing leucogranites, Sikait area, Southeastn desert of Egypt utilizing mineralogical and bulk rock analysis. *Scientific Reports, 15*(1), Article 20191. https://doi.org/10.1038/s41598-025-06155-x

Saleh, G. M., Lasheen, E. S. R., Foi, M., Abdalla, F., & Abdelaal, A. (2025). Assessment of radioactivity and heavy metal pollution levels in the coastal sediments in the Red Sea region of Sharm El Luli, Egypt. *Water, Air, & Soil Pollution, 236*(5), 319. https://doi.org/10.1007/s11270-025-07962-8

Saleh, G. M., Mohamed, G. A., & El Tohamy, A. M. (2023). Petrogenesis and geological implications of the trachytic rocks in the South Eastern Desert, Egypt: Mineralogical, geochemical, and radioactivity insights. *Applied Earth Science: Transactions of the*

Institutions of Mining and Metallurgy, 132(3–4), 194–215. https://doi.org/10.1080/25726838.2023.2244771

Satir, M., Morteani, G., Fuganti, A., & Drach, V. V. (1991). K-Ar ages, Sr-isotopic compositions and chemistry of late cretaceous-tertiary basalts from the Nubian Desert (northern Sudan). *European Journal of Mineralogy, 3*(6), 943–956. https://doi.org/10.1127/ejm/3/6/0943

Scott, A. J., & Symons, M. J. (1971). Clustering methods based on likelihood ratio criteria. *Biometrics, 27*(2), 387. https://doi.org/10.2307/2529003

Senthilkumar, G., Raghu, Y., Sivakumar, S., Chandrasekaran, A., Prem Anand, D., & Ravisankar, R. (2014). Natural radioactivity measurement and evaluation of radiological hazards in some commercial flooring materials used in Thiruvannamalai, Tamilnadu, India. *Journal of Radiation Research and Applied Sciences, 7*(1), 116–122. https://doi.org/10.1016/j.jrras.2013.12.009

Shahrokhi, A., Adelikhah, M., Chalupnik, S., Kocsis, E., Toth-Bodrogi, E., & Kovács, T. (2020). Radioactivity of building materials in Mahallat, Iran – An area exposed to a high level of natural background radiation – Attenuation of external radiation doses. *Materiales de Construcción, 70*(340), 233. https://doi.org/10.3989/mc.2020.03820

Sharaf, J. M., & Hamideen, M. S. (2013). Measurement of natural radioactivity in Jordanian building materials and their contribution to the public indoor gamma dose rate. *Applied Radiation and Isotopes, 80*, 61–66. https://doi.org/10.1016/j.apradiso.2013.06.016

Shehzad, W., Satti, K. H., Khan, M., Khan, K., Naseem, A., Ur Rehman, S., & Jabbar, A. (2019). Estimation of background radiation levels and associated health risks in mineral rich district Chiniot, Pakistan. *Journal of Radioanalytical and Nuclear Chemistry, 319*(3), 1051–1058. https://doi.org/10.1007/s10967-019-06425-9

Sherif, H. M. (1997). *Geology and uranium potentiality of wadi Seih area, southwestern sinai, Egypt. Ph.D. Thesis, geology department.* Cairo University, Faculty of Science.

Sivakumar, S., Chandrasekaran, A., Senthilkumar, G., Suresh Gandhi, M., & Ravisankar, R. (2018). Determination of radioactivity levels and associated hazards of coastal sediment from south east coast of Tamil Nadu with statistical approach. *Iranian Journal of Science and Technology, Transactions A: Science, 42*(2), 601–614. https://doi.org/10.1007/s40995-017-0184-2

Tanasković, I., Golobocanin, D., & Miljević, N. (2012). Multivariate statistical analysis of hydrochemical and radiological data of Serbian spa waters. *Journal of Geochemical Exploration, 112*, 226–234. https://doi.org/10.1016/j.gexplo.2011.08.014

Tuo, F., Peng, X., Zhou, Q., & Zhang, J. (2020). Assessment of natural radioactivity levels and radiological hazards in building materials. *Radiation Protection Dosimetry, 188*(3), 316–321. https://doi.org/10.1093/rpd/ncz289

UNSCEAR. (2000). *Sources and effects of ionizing radiation: United Nations scientific committee on the effects of atomic radiation: UNSCEAR 2000 report to the general assembly, with scientific annexes.* United Nations.

UNSCEAR. (2010). *Sources and effects of ionizing radiation: United Nations scientific committee on the effects of atomic radiation: UNSCEAR 2008 report to the general assembly, with scientific annexes.* United Nations.

Vapnik, V. N. (2000). *The nature of statistical learning theory*. New York: Springer. https://doi.org/10.1007/978-1-4757-3264-1

Wais, T. Y., Ali, F. N. M., Najam, L. A., Mansour, H., & Mostafa, M. Y. A. (2023). Assessment of natural radioactivity and radiological hazards of soil collected from rabia town in nineveh governorate (North Iraq). *Physica Scripta, 98*(6), Article 065304. https://doi.org/10.1088/1402-4896/acd732

Yıldırım, A., & Gülmez, F. (2025). Natural radioactivity and radiological hazards in ultrapotassic rocks from the Central Pontides, Türkiye. *Annals of Nuclear Energy, 223*, Article 111619. https://doi.org/10.1016/j.anucene.2025.111619

Yu, K. N., Young, E. C. M., Stokes, M. J., Luo, D. L., & Zhang, C. X. (1992). Indoor Radon and environmental gamma radiation in Hong Kong. *Radiation Protection Dosimetry, 40*(4), 259–263. https://doi.org/10.1093/oxfordjournals.rpd.a081212

Yuan, J.-M., Wang, Q.-S., Ross, R., Henderson, B., & Yu, M. (1995). Diet and breast cancer in Shanghai and Tianjin, China. *British Journal of Cancer, 71*(6), 1353–1358. https://doi.org/10.1038/bjc.1995.263

Zakaly, H. M. H., Awad, H. A., Lasheen, E. S. R., Issa, S. A. M., Elsaman, R., Khandaker, M. U., Al-awah, H., Fathy, D., & Sami, M. (2024). Radiometric and petrographic characterization of El-Yatima granite: Evaluating radiological risks and mineralogical features. *Radiation Physics and Chemistry, 224*, Article 111992. https://doi.org/10.1016/j.radphyschem.2024.111992